Title: Annexin and calcium-regulated priming of legume root cells for endosymbiotic infection

Authors:

Ambre Guillory[1§], Joëlle Fournier[1§], Audrey Kelner[1§], Karen Hobecker[2], Marie-Christine Auriac[1], Lisa Frances[1], Anaïs Delers[1], Aurélie Le Ru[3], Jean Keller[4], Pierre-Marc Delaux[4], Caroline Gutjahr[2], Nicolas Frei Dit Frey[4] and Fernanda de Carvalho-Niebel[1*]

Affiliations :

[1]LIPME, INRAE, CNRS, Université de Toulouse, Castanet-Tolosan, France.

[2]Max-Planck-Institute of Molecular Plant Physiology, Potsdam-Golm, Germany.

[3]FRAIB-TRI imaging platform, Université de Toulouse, CNRS, UPS, Castanet-Tolosan, France.

[4]LRSV, Université de Toulouse, CNRS, UPS, Toulouse INP, Castanet-Tolosan, France.

[§]these authors contributed equally to this work

[*]Correspondence to: Fernanda de Carvalho-Niebel (fernanda.de-carvalho-niebel@inrae.fr)

Abstract

Legumes establish endosymbioses with arbuscular mycorrhizal (AM) fungi or rhizobia bacteria to improve mineral nutrition. Symbionts are then hosted in privileged habitats, root cortex (for AM fungi) or nodules (for rhizobia), for efficient nutrient exchanges. To reach them, the plant creates trans-vacuolar cytoplasmic bridges, key for predicting and directing AM fungi hyphae or rhizobia-filled infection threads (ITs) entry. Yet, mechanisms underlying this pre-infection cellular remodelling are poorly studied. Here we show that unique ultrastructural changes and Ca^{2+} spiking signals closely linked to MtAnn1 annexin cellular dynamics, shape rhizobia-primed cells. Loss of *MtAnn1* function in *M. truncatula* affects peak amplitude, cytoplasm configuration and rhizobia infection, consistent with MtAnn1's role in regulating this priming state. *MtAnn1,* mainly recruited during evolution in plants establishing endosymbioses, also appears involved in the ancient AM symbiosis in *M. truncatula*. Together, our work suggests MtAnn1 as part of an ancient Ca^{2+}-regulatory module for transcellular endosymbiotic root infection.

Introduction

Plants benefit from associations with microbes in the soil which improve the acquisition of essential nutrients for growth. These associations include the ancestral symbiosis with arbuscular mycorrhizal (AM) fungi providing phosphorous supply, or the more recently evolved interactions with endosymbiotic bacteria for nitrogen acquisition[1,2]. Microbial endosymbionts are hosted in privileged intracellular niches, where optimal conditions are met for efficient nutrient exchange (e.g. the root cortex hosting arbuscules formed by AM fungi, or root nodules, hosting nitrogen-fixing bacteria). Extensive studies on model legumes such as *Medicago truncatula*, combined with evolution-based studies across broad species range revealed that nodule-forming nitrogen-fixing endosymbiosis (RNS) evolved ~100 million years ago in species from related angiosperm plant lineages, by co-opting signalling components from the ancient AM symbiosis and recruiting new key genes through neo-functionalization and/or rewiring of expression[2-4]. Remarkably, AM and RN symbioses share a common symbiotic pathway that uses calcium (Ca^{2+}) as a key secondary messenger to trigger downstream signalling[5,6]. Indeed, the perception of mycorrhizal Myc and rhizobial Nod factor signals induces Ca^{2+} oscillations (spiking) in and around the root hair nucleus through the concerted action of nuclear envelope channel/pump complexes[5-7]. While Ca^{2+} spiking is critical in the nucleus (after its decoding by Ca^{2+}/calmodulin-dependent protein kinases CCaMK or Does not Make Infection, DMI3)[8,9] to regulate host transcriptional reprogramming[10-12], the functional relevance of sustained Ca^{2+}spiking in the cytoplasmic compartment has not yet been established. The rhizobia- and AM-induced *MtAnn1*[13] and *MtAnn2*[14] genes, which encode Ca^{2+}-binding and phospholipid membrane-associated proteins of the annexin family, whose members are involved in the regulation of ionic conductance and cytoplasmic Ca^{2+} signals[15-19], are potential players in this process.

Following signal exchanges to reach compatibility, infection of root tissues by AM fungi or rhizobia bacteria occurs in most legumes transcellularly, through the *de novo* construction of apoplastic compartments, delimited by host cell wall/ membrane interfaces, which physically separate microsymbionts from the host cytoplasm[20,21]. The hyphae of AM fungi progress through epidermal and cortical root tissues until the fungus reaches the inner cortex to form

highly branched arbuscules inside plant cells. Arbuscules comprise a massive network of membrane tubules at the symbiotic host-fungus interface[22,23], which likely ensures the release of nutrients, particularly phosphate, to the plant. In RNS, rhizobia enter the roots of most legume species, *via* apoplastic tubular structures called infection threads (ITs)[21]. ITs are formed in root hairs after rhizobia have been entrapped and enclosed in a globular infection chamber, a process orchestrated by dynamic changes in the cytoskeleton-plasma-membrane-cell wall interface[24-26]. ITs grow polarly from cell to cell towards the developing nodule forming underneath[27,28], and these two programs must be tightly synchronized before a fully functional nodule is formed under the influence of key plant hormones, intercellular signalling and long-distance regulatory pathways[29-32].

There are striking similarities in the cellular events that underlie early penetration by AM fungal hyphae and rhizobia-containing ITs. In both cases, plant root cells undergo a radical reprogramming that results in the formation of characteristic cytoplasmic columns, known as Pre-Penetration Apparatus (PPA)[33] or Pre-Infection Thread (PIT)[34] to guide the transcellular passage of AM fungal hyphae and rhizobia-filled ITs, respectively. Remarkably, such endosymbiosis-related cytoplasmic remodelling is not seen in pathogen interactions[35]. Thus, a conserved and probably ancient cellular mechanism is used to commit plant cells to beneficial endosymbioses. In this process, differentiated root cells with a large central vacuole switch to an activated symbiotic state (hereafter referred to as pre-infection priming), with characteristic trans-vacuolar cytoplasmic strands radiating from the nucleus before a cytoplasmic bridge is actually formed. Parallels have been drawn between PIT/PPA and phragmosome formation in mitotically dividing cells, as similarities have been demonstrated on the tight control of the plant cell division status, membrane trafficking and microtubule dynamics during fungal and/or rhizobial infection[36-40]. The development of fluorescent protein fusions labelling the cytoplasm or endoplasmic reticulum network (ER) has made it possible to visualize the dynamics of cytoplasmic reprogramming *in vivo* during PPA and PIT formation[33,41]. These studies showed that this remodelling, guided by the nucleus, occurs in root hairs to accompany IT progression and in neighbouring cortical cells to anticipate IT passage. Primed cortical cells show a low-frequency Ca^{2+} spiking signature that switches to a high frequency at the onset of infection by AM fungi or rhizobia[42]. CCaMK is critical for endosymbiotic infection and can trigger cytoplasmic remodelling in the cortex in the absence of symbionts[43]. Thus, CCaMK-mediated signalling can bypass early symbiotic activation to trigger the priming response, at least in the cortex. These results imply that symbiotic commitment of plant cells involves fine-tuned regulation of Ca^{2+} spiking signatures, yet the underlying genetic pathways or molecular players have not been identified.

In this study, using resolutive microscopy methods in different *M. truncatula* genetic backgrounds, we provide novel insights on ultrastructural rearrangements and *in vivo* Ca^{2+} signalling dynamics in plant cells preparing for rhizobia infection. We demonstrate that this cellular reprogramming is marked by an intimate link between Ca^{2+} spiking and the annexin MtAnn1. MtAnn1 is key for shaping cytoplasmic reprograming for infection, *via* a genetic pathway controlled by the master symbiotic transcription factor Nodule Inception (NIN)[3]. Through phylogenetics and mutant phenotyping, we provide evidence that *MtAnn1*, recruited during evolution in plants establishing root endosymbioses, likely plays an ancestral role for successful rhizobia and AM fungi infection. We propose that *MtAnn1* was recruited to shape calcium-regulated transvacuolar cytoplasmic rearrangements for successful endosymbiotic root infection.

Results

Cell-specific ultrastructural changes in plant cells prior to IT entry

Previous light microscopy studies reported PIT cellular rearrangements in vetch or *Medicago* nodule or root cells[34,40]. Here, we set up an adapted methodology to gain access to ultrastructural changes underlying rhizobia pre-infection priming in *M. truncatula*. Segments of early infected roots, harvested 5-6 dpi with rhizobia, were prepared for light and transmission electron microscopy (TEM) using an Epon-embedding procedure. These analyses revealed specific cytoplasmic rearrangements in primed outer cortical cells (C1) next to an infected root hair site (Fig 1A-C). TEM analyses showed that the thick cytoplasmic bridge is highly enriched in endoplasmic reticulum (ER) (white arrows, Fig. 1E) and large quantities of small vacuole-like structures with sizes ranging from 0,5 to 5 µm (v in Fig. 1E). These activated cells also feature an unusually high density of mitochondria, often elongated, around the nucleus (m in Fig. 1E). This pre-infection priming structural configuration was never observed in other cells of the primordia, even in actively dividing meristematic cells of the C3 cell layer (Fig. 1C-D). At a later stage, when the IT has progressed across this small vacuole- and ER-rich cytoplasmic bridge, the nucleus is often found in close proximity to the IT (Fig. 1F-G). Thus, the plant nucleus not only guides the progression of ITs but also establishes close physical interactions with them. Overall, drastic, cell-specific ultrastructural changes take place in outer cortical cells primed for rhizobia infection, which are marked by a unique transcellular cytoplasmic organization, enriched with ER, small vacuole-like structures and perinuclear mitochondria.

MtAnn1 and Ca^{2+} spiking dynamics mark symbiotically engaged and infected plant cells

MtAnn1, encoding a Ca^{2+} and membrane phospholipid binding annexin protein, is expressed in outer cortical cells preparing for rhizobia infection[13], where coincidently Ca^{2+} spiking responses are transiently regulated[42]. To assess if these two responses are functionally interconnected, we set up a new *in vivo* strategy aimed at monitoring both responses simultaneously in individual root cells. Co-expression of a red fluorescent NR-GECO1 nuclear calcium sensor[44] and a green fluorescent MtAnn1-GFP fusion was therefore used to live track the spatio-temporal dynamics of Ca^{2+} spiking and MtAnn1 in (i) non-infected, Nod factor-responsive root hairs of the nodulation susceptible zone, (ii) infected root hairs in the proximal root region and (iii) adjacent primed cortical cells. These challenging analyses were performed in *M. truncatula* A17 (wild-type, WT) and in the *sunn2* mutant[45]. This mutant, which shows wild-type infection events but in greater numbers, is optimal for live imaging studies of early rhizobia infection events[24,27,46].

Periodic, high frequency, Ca^{2+} oscillations resembling those induced by purified Nod factors[44], are observed in most root hairs of the nodulation susceptible zone as early as 12 h post-inoculation with *Rhizobia* in both *sunn2* and A17 (Supplementary Fig. S1 and Movies 1-2 show control and rhizobia-inoculated WT root hairs at 1 dpi). Double labelling of MtAnn1-GFP and NR-GECO greatly facilitated detection of root hairs in early stages of bacterial entrapment (RHE) and IT polar growth. Indeed, infected root hairs show both Ca^{2+} spikes and MtAnn1-GFP fusion expression (Fig. 2). However, MtAnn1-GFP expression levels were clearly higher in root hairs containing growing ITs compared with RHE root hairs (Fig. 2A-B). On the other hand, the amplitude of Ca^{2+} spikes drops significantly in IT compared to RHE stages (Fig. 2C-E), while Ca^{2+}

spiking frequency is not significantly altered (Fig. 2F). Overall, our data show that a decrease in Ca^{2+} spiking amplitude and a rise in MtAnn1 expression are associated with polar IT growth.

In addition to accompanying rhizobial entry in root hairs, MtAnn1-GFP fusion expression is also observed in outer cortical cells adjacent to a root hair infection site at 3-4 dpi with rhizobia (Fig. 3A-C). This labelling is specific to one or a few cells around the infection site (Fig. 3A-C). Strikingly, these MtAnn1-labelled cells consistently show low frequency Ca^{2+} spiking, whereas nearby cells not labelled with MtAnn1 do not show any Ca^{2+} spiking (Compare C1a-c in Fig. 3). This data establishes a direct link between symbiotic priming, MtAnn1 expression and low frequency Ca^{2+} spikes. Together, this data indicates that priming for infection and IT development are guided by cell type and stage-specific Ca^{2+} spiking signatures that are closely linked with MtAnn1 dynamics.

Rhizobia root hair entrapment is required for pre-infection priming of adjacent cortical cells

MtAnn1-GFP labelling and Ca^{2+} spiking mark symbiotically primed outer cortical cells (C1 in Fig. 3C), however it is unclear if formation of a root hair IT is required before these responses are activated. To gain insight into the genetic components underlying pre-infection priming, we studied how these responses are triggered in IT-defective plant mutants transformed with NR-GECO1 and/or the MtAnn1-GFP fusion.

The *M. truncatula ern1* (for ERF Required for Nodulation 1) mutant is defective in IT development in root hairs, but is still able to form root hair infection chambers with entrapped bacteria[47,48]. This mutant shows Ca^{2+} spiking and cytoplasmic-bridge formation (visualized with MtAnn1-GFP) in early infected root hairs (Fig. 3D and Supplementary Fig. S2A and D). Pre-infection priming in cells adjacent to an infected root hair site is also well visualized in this mutant. Indeed, primed cells, with characteristic cytoplasmic strands radiating from the central nucleus, marked with MtAnn1-GFP fluorescence and showing Ca^{2+} spiking responses, are clearly distinguished in *ern1* (Fig. 3D and Supplementary Fig. S2B-D). Thus, despite being defective in root hair IT growth, priming of neighbouring cells is still triggered in *ern1*. However, while pre-infection priming is limited to a few adjacent cortical cells in WT and *sunn2* backgrounds, it is strikingly deregulated in *ern1* (Fig. 3 and Supplementary Fig S2B-C). Priming responses in *ern1* are exaggerated as they are seen in extended regions of MtAnn1-GFP-labelled epidermal and cortical cells. These cells show coordinated low frequency Ca^{2+} spiking (as in the WT background, Fig. 3) or unusual high-frequency patterns (Supplementary Fig 2C-D). This suggests that ERN1 is not required for promoting pre-infection priming, but is somehow required to spatially restrict it.

The *ern1 ern2*[48] and *dmi3*[8] mutants, which are totally deficient in root hair bacterial entrapment and infection, show Ca^{2+} spiking in root hairs ([49] and Supplementary Fig S2E and Movie 3) but no clear signs of cytoplasmic remodelling in root hairs or cortical cells. Moreover, these root hairs show only residual (in *ern1 ern2*) or no (in *dmi3*) MtAnn1-GFP expression. Thus, the formation of MtAnn1-labelled cytoplasmic bridges, characteristic of primed cells, seems to require the formation of rhizobia root hair infection foci. To test this hypothesis, we investigated if complementation of *dmi3* with a epidermal-expressed (*pEXT:DMI3*) fusion, that can rescue IT development in *dmi3* root hairs[50], could restore cytoplasmic bridge formation. While MtAnn1-labelled cytoplasmic bridges were strongly detected in infected root hairs of complemented *dmi3*, no pre-infection priming events were observed in adjacent cortical cells

(no signs of MtAnn1 labelling, Ca^{2+} spiking or cytoplasmic remodelling, Supplementary Fig S2E-F). This suggests that PIT-related infection priming uses a DMI3-dependent signalling pathway.

Overall, our mutant analyses indicate that the formation of rhizobia infection foci in root hairs is sufficient to trigger the formation of strongly MtAnn1-GFP-labelled cytoplasmic bridges in root hairs and in adjacent cortex. Overactive (in *ern1*) and absent (in *dmi3*) priming responses in adjacent cells are consistent with the conclusion that pre-infection priming is genetically-dependent on DMI3, and under tight spatial control by ERN1.

NIN controls pre-infection priming and the associated expression of *MtAnn1*

The master symbiotic transcription factor Nodule INception (NIN) is genetically placed downstream of DMI3 and its mutation abolishes rhizobia-induced *MtAnn1* expression[51], raising the question of its implication in *MtAnn1* regulation and pre-infection priming. To test if NIN is indeed required for symbiotic *MtAnn1* expression, we compared the spatio-temporal expression profile of a *pMtAnn1:GUS* fusion in WT and *nin* genetic backgrounds. As shown in Fig. 4A-C, strong expression of the *pMtAnn1:GUS* fusion is observed at rhizobia infection sites in WT but not in *nin* roots, confirming the genetic dependence on NIN to confer infection-related *MtAnn1* expression. Conversely, expression of NIN under the epidermis-specific *pEXPA* promoter[52] in *nin* induces *pMtAnn1:GUS* fusion expression in the epidermis in the absence of rhizobia (Fig. 4D). This indicates that NIN can bypass early symbiotic signal transduction to directly activate the *pMtAnn1:GUS* fusion. Transactivation studies in *Nicotiana benthamiana* cells (Fig. 4E and Supplementary Fig. S3), confirmed the ability of NIN to transcriptionally activate the *pMtAnn1:GUS* fusion (Fig. 4E). This activation is no longer observed when NIN is deleted in its DNA binding domain (Fig. 4E). These data establish NIN as a likely direct regulator of *MtAnn1*.

Besides abolishing *MtAnn1* expression, *nin* fails to form proper infection chamber and ITs but can still entrap rhizobia within a deformed root hair[24]. However, it is unclear if PIT-like cytoplasmic remodelling can still be initiated in *nin*. To investigate that, the *in vivo* dynamics of a fluorescent GFP-ER fusion was live tracked in *nin* complemented or not in the epidermis by the expression of a *pEXPA:NIN* construct (Fig. 4F-K). In *nin*, the GFP-ER fluorescent fusion marks the ER network and associated cytoplasm, mainly visualized around the nuclei and in growing root hair tips. However, no cytoplasmic columns are detected in this genetic background (Fig. 4F). *pEXPA:NIN*-complemented *nin* root hairs, recognized by red fluorescent Ds-Red nuclei, show thick GFP-labelled cytoplasmic columns in infection chamber-forming root hairs (Fig. 4G-H). However, outer cortical cells from *nin* (complemented or not) show no signs of priming, as evidenced by the absence of GFP-ER or Ds-Red-labelled associated cytoplasmic remodelling (Fig. 4I-K). This suggests that a functionally active NIN is required in the cortex to trigger infection-related cytoplasmic remodelling. Taken together, these data suggest that NIN acts downstream of DMI3 to control pre-infection priming and the associated expression of *MtAnn1*.

MtAnn1 mutation impacts nodule differentiation and function

To evaluate the relative importance of *MtAnn1* for nodulation, phenotypic analyses of three available *M. truncatula Tnt1* R108 insertion mutant lines were undertaken (Supplementary Fig. S4A). These lines, containing insertions in the promoter (*ann1-1*) or

exonic regions of *MtAnn1* (*ann1-2* and *ann1-3*), show reduced (*ann1-1*) or almost abolished (*ann1-2* and *ann1-3*) rhizobia-induced expression of *MtAnn1* compared with WT lines (the R108 background and WT siblings from the same mutagenized population) (Supplementary Fig. S4B). Phenotyping of *ann1-2* and *ann1-3* did not reveal any major changes in root architecture or nodule number compared with the WT lines at 21 dpi (Supplementary Fig. S4C-F). However, nodules formed in mutant roots showed striking variations in their shape (less elongated overall) and colour (paler pink) (Fig. 5A-C and Supplementary Fig. S4D-F), reminiscent of potential differentiation and/or nitrogen fixation defects[53]. Indeed, comparison of nodule shape in *ann1-3* and WT, by calculating the length to width ratio of individual 21 dpi nodules, revealed significant differences between the two genotypes (Fig. 5D). An automated Image J quantification system (see Methods) confirmed nodule size differences in the *ann1-2* and *ann1-3* mutants compared with WT lines at 10 dpi (Fig. 5E).

To better understand why *ann1* mutant nodules were smaller and less elongated, we performed a detailed analysis of thin and ultrathin sections of WT and *ann1-3* nodules (Fig. 5G-N). Meristematic (I), infection (II), amyloplast-rich interzone (IZ) and nitrogen fixation (III) zones are clearly distinguished in WT nodules (Fig. 5G and I). However, *ann1-3* nodules show an abnormally large IZ like region, with over-accumulation of amyloplasts and less clearly defined zone III (Fig. 5H and J). TEM analyses showed that zone III of WT nodules comprised, as expected, uninvaded cells (UC) interspersed with invaded cells (IC) filled with nitrogen-fixing bacteroids, the latter with low numbers of amyloplast grains located near intercellular spaces (Fig. 5K and M). Although *ann1-3* nodules include IC cells with apparent differentiated bacteroids (Fig. 5L, N), they comprise small vesicles (asterisks in Fig. 5N) that are normally found in IZ rather than zone III of WT nodules[54]. This supports the general conclusion that *ann1-3* nodules are unable to differentiate effectively into a fully functional nodule with a defined zone III. As a result, *Mtann1* mutant nodules have decreased nitrogen fixation abilities (Fig. 5F), which ultimately results in slightly reduced plant growth (Supplementary Fig. S4D). The amyloplast-related phenotype of *ann1-3* is linked to increased expression of a gene encoding an interzone-associated starch synthase, and this phenotype can be partially restored in complemented roots (Supplementary Fig. S5). These results imply that starch accumulated during early stages of nodule development is not properly metabolized in *MtAnn1* mutant nodules. Taken together, these results indicate that *Mtann1* mutant nodules are affected in their ability to differentiate and fix nitrogen.

MtAnn1-dependent modulation of Ca^{2+} spiking and cytoplasmic ultrastructural organization for efficient rhizobia infection

As *MtAnn1* expression is tightly associated with early stages of rhizobial entry, we aimed to determine the impact of *MtAnn1* mutation in rhizobial infection. We assessed this by monitoring bacterial β-galactosidase reporter activity (in blue) in inoculated root and nodule tissues. Root hair ITs are formed in mutant roots at 4 dpi with rhizobia, but at a lower frequency compared with WT (Fig. 6A). A lower proportion also reach the outer cortex (OC) and fully colonize emerging nodule primordia (NP) or nodules at 4 and 10 dpi with rhizobia (Fig. 6B-K). Mutant nodule primordia are often colonized by multiple ITs compared with the control (Fig. 6D-E and J), suggesting an inefficient process. Complementary RNAi knockdown of *MtAnn1* in *M. truncatula* A17 also results in reduced nodule primordia colonization at 5 dpi with rhizobia (Supplementary Fig. S6). Thus, impaired *MtAnn1* function in mutant and RNAi contexts affects rhizobia root and nodule infection in different *M. truncatula* genotypes.

As Ca^{2+} spiking and MtAnn1 dynamics are closely linked in peri-nuclear regions of primed cells (Fig. 2-3), we decided to assess if *MtAnn1* mutation could somehow impact symbiotic Ca^{2+} spiking. WT and *ann1-3* transgenic roots expressing the NR-GECO1 Ca^{2+} sensor, were used to monitor these responses. Although more challenging than previous live analysis in the hyperinfectious *sunn2* context (Fig. 2), we observed the same drop in Ca^{2+} spiking amplitude in IT-containing RHs compared with RHE root hairs in the WT context (Fig. 7A). However, this decrease is no longer observed in *ann1* mutants (Fig. 7B). Likewise, a deregulated Ca^{2+} spiking amplitude pattern is also observed in *S. meliloti*-responsive root hairs of *ann1-3* compared with WT while Ca^{2+} spiking frequency is not significantly changed in any root hair categories (Fig. 7C and Supplementary Fig. S7). Together, these data indicate that *MtAnn1* is required for modulating symbiotic Ca^{2+} spiking responses.

Ca^{2+} spiking and MtAnn1 dynamics accompany cytoplasmic bridge formation (Fig. 2-3), so we wondered how *MtAnn1* mutation and deregulated Ca^{2+} spiking amplitude in *ann1-3* (Fig. 7) could affect cytoplasmic bridge formation. We thus analysed the cytoplasmic composition of infected cells in apical nodule zones of WT and *ann1-3* by resolutive TEM. As similarly shown in A17 (Fig. 1), ITs in R108 WT progress through a small vacuole-like enriched cytoplasmic bridge comprising a dense ER network (Fig. 7D-E and H-I). In *ann-1-3*, this small vacuole-like and ER-rich environment is no longer observed in the cytoplasmic compartment around the IT (Fig. 7F-G and J-K). Thus, mutation in *MtAnn1* results in a deregulated Ca^{2+} spiking response and a change in the ER and vesicle composition of the remodelled cytoplasmic bridge. We thus hypothesise that MtAnn1, as a calcium and membrane binding cytoplasmic annexin protein, is required to modulate Ca^{2+} spiking signatures, likely needed to structurally organize the cytoplasmic bridge for proper IT progression.

***MtAnn1* is required for proper mycorrhizal root colonization**

Recently developed genomic and transcriptomic databases from around 300 plant species establishing different types of endosymbioses make it now possible to address key endosymbiosis-related ancestral gene functions[55]. We have thus exploited these extensive resources to trace the evolutionary history of *MtAnn1*. Previous studies of the monophyletic plant annexin group, mainly composed of angiosperm sequences, suggested their emergence through duplications from a common ancestor prior to the monocots/eudicots split[56]. Consistent with these data, we found that the *MtAnn1* annexin cluster likely arose from sequential pre-angiosperms, eudicots and Papilionoideae-specific duplications (Supplementary Fig S8). *MtAnn1* belongs to one of the Papilionoideae duplicated clades, which includes mainly species that establish intracellular endosymbioses (Supplementary Fig. S8), with the exception of *Caryophyallae* and *Cephalotus* (status uncertain). In particular, *Ann1* orthologs were also detected in Papilionoideae species that have lost RNS but maintain the AM symbiosis. This indicates that the function of *Ann1* is not restricted to RNS but could expand to the AM symbiosis. Strikingly, *MtAnn1* from different species show consistent transcriptional activation during both root nodule symbiosis and the ancient AM symbiosis, suggesting an ancestral role in root endosymbiotic infection[4]. To determine if this was the case, we first decided to assess if *MtAnn1* promoter activity was spatio-temporally regulated in *M. truncatula* roots colonized by the AM fungus *Rhizophagus irregularis*. Strong activation of a *pMtAnn1:GUS* fusion was observed in root segments colonized by *R. irregularis* at 4 wpi,

especially in cortical cells containing arbuscules (Fig. 8A-B), consistent with an important role for *MtAnn1* in AM symbiosis development. To assess that, we compared the percent root length colonization of WT and *ann1-3* mutant roots colonized by *R. irregularis*. At 6 wpi, WT roots showed, as expected, root segments densely colonized by *R. irregularis*, with cortical cells fully filled with arbuscules (Fig. 8C, E and F). The mutant roots, on the other hand, were significantly less colonized (Fig. 8C, G and H). They not only had a lower proportion of colonized root sectors (Fig. 8C), but the arbuscule density was also reduced (Fig. 8D). These data highlight the involvement of *MtAnn1* in the ancient AM symbiosis and suggest its ancestral recruitment for successful colonization by endosymbiotic microbes.

Discussion

Endosymbiotic root infection by rhizobia occurs in most legumes transcellularly, through the creation of IT apoplastic structures that grow polarly to reach the developing nodule. Plant cells engage symbiotically in this process by creating characteristic trans-vacuolar PIT cytoplasmic bridges, which shape the cellular route for IT progression. PITs, along with analogous PPA structures formed during infection by AM fungi, are likely governed by common ancestral cellular mechanisms, though knowledge remains limited to date. In this manuscript, we uncover cell-specific ultrastructural rearrangements and stage and cell-specific Ca^{2+} responses that prime *M. truncatula* plant cells for endosymbiotic infection by rhizobia. We show that pre-infection reprogramming is marked by an intimate link between Ca^{2+} spiking and the annexin MtAnn1, which together integrate the so-called primed cellular state, induced in dependence of a DMI3-NIN-controlled genetic pathway. We discovered MtAnn1 as a novel regulator of symbiotic Ca^{2+} spiking amplitude. Also, MtAnn1 plays an important role in the creation of a dense, ER- and small vacuole-rich cytoplasmic environment, propitious for successful rhizobial infection. This study also shows that *MtAnn1* is needed for successful formation of nitrogen-fixing nodules by rhizobia and root cortical arbuscules by AM fungi. Alongside the ancient recruitment of *MtAnn1* in plants establishing endosymbioses, experimental evidence from this work suggests the functional importance of *MtAnn1* in driving efficient Ca^{2+}-regulated trans-vascuolar cytoplasmic bridge formation for successful endosymbiotic root infection.

Organelle dynamics shaping rhizobia pre-infection priming

Dissecting the ultrastructure of plant cells preparing for transcellular rhizobia infection revealed the marked enrichment and spatial re-distribution of organelles during this process (Fig. 1). This pre-infection priming state is only visible in a few outer cortical cells prior to IT entry (Fig. 1 and 3), underlining a tight cell-specific regulatory control. As reported during PPA formation[33], mitochondria enrichment is observed in these primed cells (Fig. 1), perhaps reflecting the highly energy-demanding nature of these processes. Nevertheless, perinuclear clustering of mitochondria is not prevalent in surrounding root cells, not even in C3 meristematic cells with presumably high metabolic activity (Fig. 1). Of note, the distribution of mitochondria around the nucleus appears to be dynamically regulated during cell cycle transitions in *A. thaliana*[57]. As cells undergoing or preparing for rhizobia infection are under tight cell cycle control[37,39], this mitochondrial pattern may reflect a unique cell-cycle activation status of primed cells. Mitochondria perinuclear clustering could also simply reflect the dense

cytoplasmic clustering around the nucleus. Nevertheless, as mitochondria play emerging roles in modulating cytoplasmic Ca^{2+}signals in plants[58], it is tempting to speculate if their clustering in the perinuclear region, where dynamic calcium oscillations occur, could have regulatory implications in the symbiotic Ca^{2+} response.

Previous studies showed that the transcellular cytoplasm of rhizobia primed cells is shaped by microtubule bundles and decorated by an ER network[38,40,41]. Our TEM analysis provided ultrastructural evidence that a dense ER-rich network occupies the transcellular cytoplasmic bridge in *M. truncatula* root cells either primed or rhizobia infected (Fig. 1 and Fig. 7). This region is also rich in small vacuole-like structures, but we cannot definitely determine if these are fragmented or small, newly-formed, vacuoles[59]. Also, we were unable to detect an enrichment in multivesicular bodies (MVBs) seen in PPA[60] perhaps masked by the prominent vacuoles. Nevertheless, a functional link may exist here as small vacuoles can derive from MVB fusion[59]. Small vacuole-like structures are also observed in PPA, in dividing cells or sub-apical regions of growing root hairs[59,60,75]. As the ER represents the gateway to intracellular trafficking and the main source for vacuole biogenesis[61], the ER and small vacuole-enriched pattern of primed cells is suggestive of an active vesicle fusion and/or vacuole biogenesis process, in which the annexin MtAnn1 appears to be an important component, as discussed hereafter.

Role of MtAnn1 in modulating cell- and stage-specific symbiotic Ca^{2+} responses

High frequency Ca^{2+} spiking, triggered by Nod factors in root hairs of the nodulation competence zone, is central for early recognition of rhizobia[5,6,44]. Here, we showed that a second Ca^{2+} spiking phase occurs in root hairs undergoing rhizobia infection, and involves a decrease in Ca^{2+} peak amplitude as ITs extend into root hairs (Fig. 2). This drop was also reported to occur in root cortical cells crossed by an IT[42], consistent with the hypothesis that this regulatory switch is key for IT progression in the cell. Regulation of Ca^{2+} amplitude is known to finetune different biological processes, from gene expression regulation, stomatal closure to gravitropic response, and even synaptic plasticity in animals[62-64]. The deregulated Ca^{2+} amplitude profile and defective infection caused by *MtAnn1* mutation (Fig. 6 and 7) supports the need for such a strict control and establish a direct functional link between MtAnn1 and the regulation of Ca^{2+} spiking amplitude during rhizobia infection.

Symbiotic Ca^{2+} spiking is generated in the nucleoplasm and perinuclear cytoplasm in *Medicago* by the concerted action of nuclear envelope ion channels (DMI1, CNGC15), a Ca^{2+} pump (MCA8), and under negative feedback regulation by a nuclear calmodulin (CaM2)[5,65]. MtAnn1, as a cytosolic protein, is unlikely to be among the top Ca^{2+} spike-generating proteins, but clearly contributes to moderate the signal amplitude. MtAnn1 is a phospholipid- and Ca^{2+}-interacting protein of the annexin family[13], viewed as dynamic cytosolic regulators that associate to membranes when intracellular Ca^{2+} levels change[15]. Members of the annexin family have been implicated in the regulation of ion transport, modulation of cytoplasmic Ca^{2+} signals and ROS signalling in diverse abiotic or biotic responses[16-19,66]. Even though annexins are predominantly cytoplasmic, they can also topologically associate with the ER[67,68] and modulate the activity of Ca^{2+}-release channels[69]. As MtAnn1 seems to partially co-localize with the peri-nuclear ER network in symbiotically activated cells, it could mechanistically play such a regulatory role, which would explain the disturbed Ca^{2+} signals and ER phenotypes caused by the *MtAnn1* mutation.

We determined that Ca^{2+} spiking and strong MtAnn1-GFP labelling are hallmarks of rhizobia pre-infection priming (Fig. 3) and rely on cell-autonomous activity of DMI3, as PPA formation[35,43] and NIN. These findings corroborate that spatially distinct Ca^{2+} spiking responses are triggered, first by Nod-factors in non-infected root hairs independently of DMI3-NIN, before infection-related Ca^{2+} spiking is induced in a DMI3-NIN-dependent fashion in cells engaged for infection. The latter appears to require successful infection chamber formation (seen in *ern1* not in *ern1 ern2*, *dmi3*, *nin*, Fig 3), supporting the hypothesis that rhizobia entrapment and proliferation in the chamber are pre-requisites for pre-infection priming. Moreover, ERN1 spatially restricts this process to a few cells (Fig. 3), perhaps key to delimiting the cellular route of IT passage. In agreement with previous results[42], we observe unique low frequency Ca^{2+} spiking only in primed cells of the cortex (Fig. 3). Although root hairs exhibit similar remodelling and MtAnn1 labelling responses, they do not show low frequency Ca^{2+} spiking. Thus, this Ca^{2+} signature is probably not reflecting a generalized commitment to infection but rather a specific state of cortical cells, possibly linked to their positioning at a distance from the root hair infection site.

Functional implications of MtAnn1 in organising the dense IT-associated cytoplasmic bridge

The radical alteration in the cytosolic distribution of the ER and small vacuoles by the *MtAnn1* mutation (Fig. 7), establishes a strong functional link between *MtAnn1* and the generation of this specific cytoplasmic configuration. Ca^{2+} orchestrates membrane trafficking and fusion, while vacuoles, emitters and receivers of Ca^{2+}signals, can be directly affected by altered levels of cytosolic calcium[70,71]. Pollen germination is driven by interconnected calcium oscillations and exocytosis[72], so a similar scenario is conceivable in primed cells. Annexins are among Ca^{2+} sensing proteins involved in endomembrane trafficking in plants[73], either acting in conjunction with the membrane fusion machinery or regulating exocytosis. Thus, MtAnn1 may directly or indirectly impact Ca^{2+}-regulated vesicle trafficking and/or vacuole morphology. However, the biological relevance of such a dense cytoplasmic strand for IT passage remains to be determined. Modulation of vacuole shape and distribution is used to optimize stomatal aperture, root hair development and presumably to spatially accommodate the future cell plate structure in dividing cells[74]. By analogy with the latter, dynamic shrinking of vacuoles in primed cells may be used to accommodate the future passage of the IT. A parallel can also be drawn with the similar reorganisation of a dense cytoplasmic region, rich in ER and small vacuoles, in the subapical zone of growing root hairs, in which the dense organelle arrangement appears to impact the speed of cytoplasmic streaming[75,76]. It is thus conceivable that ultrastructural cytoplasmic alterations in primed cells may somehow be needed to create an optimal streaming rate for IT growth.

Evolutionary recruitment of *MtAnn1* for root endosymbioses

Through analysis of insertional mutants, we demonstrated the importance of *MtAnn1* for proper infection and differentiation of nitrogen fixing nodules (Fig. 5). In these mutants, rhizobia root infection is reduced (Fig. 6) and this impairment culminates in mature nodules with decreased size and altered shapes, reminiscent of the reduced infection levels and nodule sizes observed in *Phaseolus* RNAi knock-down of *PvAnn1*[77]. Microscopy analysis also revealed strong differentiation phenotypes in *MtAnn1* mutant nodules, marked by a defect in

differentiation of nodule zone III, enhanced starch accumulation and overall diminished nitrogen fixation ability (Fig. 5). These phenotypes are probably a consequence of the early deregulated Ca^{2+} spiking, impaired cytoplasmic configuration and consequently defective infection caused by the *MtAnn1* mutation. During nodule primordia development, infection progression must be tightly synchronized with nodule organogenesis[30]. A possible slowdown of IT progression in the mutant may thus directly impact synchronization, resulting in impaired nodule differentiation.

A striking defect in mutant nodules is the marked overproduction of amyloplasts (Fig. 5), as previously observed in other nitrogen fixation defective nodules[53]. Starch is normally consumed in both infected and uninfected cells to fuel the differentiation of infecting bacteria into nitrogen-fixing bacteroids. This abnormal pattern, never seen in WT background, is probably not due to a simple delay in the nodule differentiation process, but rather reflects an irreversible defect created by *MtAnn1* mutation. The close paralogue *MtAnn2*[14] is unlikely to compensate for the loss of function of *MtAnn1* in nodules, as it has a distinct spatial expression profile.

We showed that the *MtAnn1* annexin cluster emerged mainly in plant species establishing intracellular symbioses. The induced expression of *MtAnn1* in rhizobia and AM symbioses and its requirement for proper formation of nitrogen-fixing nodules and cortical arbuscules (Fig. 5 and 8) suggest ancestral and common roles of *MtAnn1* for endosymbiotic infection. We propose that *MtAnn1* fine-tunes oscillatory Ca^{2+} responses for creating an optimal dense cytoplasmic environment for rhizobia IT and AM fungi hyphae progression. *MtAnn1* is regulated by NIN during rhizobia symbiosis (Fig. 4), we thus hypothesize that its evolutionary recruitment for nodulation involved the acquisition of putative NIN *cis*-regulatory motifs which are indeed present in the *MtAnn1* promoter. As NIN is specifically involved in nodulation[3], it is likely that AM-associated regulation of *MtAnn1* is mediated by another, yet unidentified, regulator.

In conclusion, we showed that cell-specific Ca^{2+} spiking signals shape rhizobia pre-infection priming to prepare the optimal dense cytoplasmic environment for IT passage in *Medicago*, and MtAnn1 emerges as a key modulator of this process. MtAnn1, necessary for proper nodule and AM development, was possibly recruited during evolution to integrate an ancestral Ca^{2+}-regulatory module for guiding endosymbiotic root infection. MtAnn1 includes a K/H/RGD motif[15], possibly interacting with C2-domain Ca^{2+}-binding proteins, and further exploration of associated protein interactors should help uncover other critical components in this process.

Methods

Plant materials and microbial strains

M. truncatula Jemalong A17 and R108 wild-type ecotypes, as well as *sunn-2*[45], *dmi3-1*[8], *nin-1*[78] and *ern1* & *ern1 ern2*[47,48] mutants were used in this work. The *dmi3* line carrying the *pEXT:DMI3* construct[50], hereafter called *dmi3* + *pEXT:DMI3*, was kindly provided by C. Remblière (LIPME, Toulouse). The three R108 *Tnt1* mutants carrying insertions in *MtAnn1* were obtained from Oklahoma State University (details in Supplementary Fig. S4) and are designated *ann1-1* (NF0830), *ann1-2* (NF17737) and *ann1-3* (NF4963). These lines were self-crossed and genotyped by PCR and sequencing at each generation using primers *-344*

pMtAnn1-Fw, *Mtr14183-Rev*, -914 *pMtAnn1-Fw*, *LTR6-* and *LTR4-* (Supplementary Table S1). Homozygous mutants and sibling wild-type lines (referred to as WT) were selected for seed multiplication and phenotyping. WT used in Fig. 5 to 8 are WT siblings derived from line NF4963. Seeds were scarified and surface-sterilized prior to germination on inverted soft agar plates[46] and used for *A. rhizogenes* transformation or nodulation experiments. *N. benthamiana* seeds were germinated in potting soil in glass-covered trays before transfer to pots (7 cm x 7 cm x 6.5 cm) at 21°C in a growth chamber under a 16h photoperiod and 70 µE/m/s light intensity for 3 weeks until bacterial infiltration. The strains *A. rhizogenes* ARquA1, *A. tumefaciens* GV3103 & GV3101 and *S. meliloti* 2011 (*Sm*2011-lac), constitutively expressing a *hemA-lacZ* fusion, were described[46]. The *S. meliloti* 2011 strain *Sm*2011-cCFP, constitutively expressing a cyan fluorescent protein was kindly provided by P. Smit, Wageningen (The Netherlands). *R. irregularis* spores (DAOM197198) were purchased from Agronutrition (Labège, France).

DNA constructs

pMtAnn1:MtAnn1-GFP[13] and *pENOD11:GFP-ER*[41] in pBIN121 were used to study live pre-infection priming responses in *M. truncatula*. *p2x35S:NR-GECO1* in pCAMBIA-CR1ΔDs-Red[44] was used to monitor Ca^{2+} spiking in *M. truncatula*. *pMtAnn1:GUS* in pLP100[13], *pEXPA:NIN* in pK7WG2-R, *p35S:3xHA-NIN* and *p35S:3xHA-NINΔ* in PAM-PAT35S-3xHA-GTW[52], were used in transcription activation studies in *M. truncatula* or *N. benthamiana*. *p35S:MtAnn1-GFP* and *p35S:GFP* in pBIN121[13], were used in mutant complementation studies. The *pMtAnn1:RNAi-MtAnn1* and *pMtAnn1:GUS* (control) constructs were generated here by Golden-Gate cloning into the pCambia-CR1 vector[44]. Briefly, DNA fragments corresponding to 2,2 kb *MtAnn1* sequences upstream of the ATG, 942 bp of *MtAnn1* coding sequence in sense and antisense orientations and the GUS coding sequence, were generated by PCR amplification using the primer pairs *pMtAnn1-GG-A-Fw*/*pMtAnn1-GG-B-Rev*, *MtAnn1-ATG-GG-B-Fw*/*MtAnn1-STOP-GG-C-Rev*, *MtAnn1 antisens-STOP-GG-X-Fw*/*MtAnn1 antisens-ATG-GG-D-Rev* and *GUS-GG-B-Fw*/*GUS-GG-D-Rev*, respectively (Supplementary Table S1). DNA fragments were then cloned into a pBluescript SK vector and validated by DNA sequencing prior to Golden Gate assembly. Golden-Gate reactions with plasmids comprising (i) the *MtAnn1* promoter, *MtAnn1* coding sequences (sense and antisense) and a 1,3 kb intron spacer[29] or (ii) the *MtAnn1* promoter and the *GUS* coding sequence, were used to generate *MtAnn1* RNAi (*pMtAnn1:MtAnn1 sens-intron-MtAnn1 antisens*) or GUS control (*pMtAnn1:GUS*) constructs in the binary pCambia-CR vector. All binary vectors used for *A. rhizogenes* transformation of *M. truncatula* (pLP100, pCambia, pK7WG2-R, pBIN121) include a kanamycin resistance cassette in the T-DNA region. pK7G2-R and pCambia-CR1 vectors also include a Ds-Red cassette.

Generation of *M. truncatula* transgenic material

A. rhizogenes-mediated transformation of *M. truncatula* A17 (WT, *sunn-2*, *ern1*, *ern1 ern2* and *dmi3*) or R108 (WT sibling and *ann1-3*) was performed as described[46]. Briefly, germinated seedlings had their root tips removed with a scalpel and were placed on Fahraeus medium plates (12 cm x 12 cm) supplemented with 0.5 mM NH_4NO_3 and 20 mg/L kanamycin, before inoculation with a drop (~3 µL) of *A. rhizogenes* aqueous suspension (OD_{600nm} 0.5). For co-transformation experiments with strains *pMtAnn1:MtAnn1-GFP + p2x35S:NR-GECO1, p2x35S:NR-GECO1 + pENOD11:GFP-ER, pEXPA:NIN + pENOD11:GFP-ER or pEXPA:NIN +*

pMtAnn1:GUS (in pLP100), equal volumes of bacterial suspensions were mixed prior to seedling inoculation. The lower ¾ part of the plates were sealed with parafilm and placed vertically in plastic boxes under controlled 16h light/ 8h dark photoperiod conditions, first at 20°C for 1 week, then at 25°C for two to three weeks. Composite *M. truncatula* plants with kanamycin resistant roots were selected. In some experiments, kanamycin-resistant composite roots were re-selected on the basis of constitutive fluorescence of the Ds-Red marker (for pK7WG2-R *pEXPA:NIN* and pCAMBIA-CR1 *pMtAnn1:RNAi-MtAnn1* and *pMtAnn1:GUS* constructs), fusion fluorescence in lateral roots (for *pMtAnn1:MtAnn1-GFP* and *pENOD11:GFP-ER* constructs) or in the nucleus (for *p2x35S:NR-GECO1*). Selected composite plants were then transferred to appropriate nitrogen- and antibiotic-free plates or pots for subsequent microbial inoculation.

Plant growth and microbial inoculation procedures

For *in vivo* imaging experiments, kanamycin-resistant and fluorescent-positive composite plants of A17 (WT, *sunn-2*, *ern1*, *ern1 ern2* and *dmi3*) or R108 (WT sibling and *ann1-3*) carrying *pMtAnn1:MtAnn1-GFP* + *p2x35S:NR-GECO1, pEXPA:NIN* + *pENOD11:GFP-ER* or *p2x35S:NR-GECO1* + *pENOD11:GFP-ER* constructs were transferred to nitrogen-free Fahraeus plates supplemented with Amoxycillin sodium/Clavulanate potassium 5:1 (200 mg/L) for 3-7 d, then transferred to nitrogen-free 0.5% [w/v] phytagel Fahraeus plates supplemented with 50nM 2-amino ethoxyvinyl glycine (AVG) for 3 d as described previously[24]. Whole root systems were then inoculated with 0.5 to 1 mL of the *Sm*2011-cCFP suspension (OD_{600nm} 0.001), applied between the medium and the LUMOX film. The inoculated root systems were kept protected from light, by wrapping ¾ of the plates with dark plastic bags in a culture room at 20°C or 25°C with a 16-h photoperiod and a light intensity of 70 mE/s/m^2, until microscopy observations.

For high-resolution microscopy analyses of pre-infection priming in A17 and nodule differentiation in WT/*ann-3*, germinated seedlings of *M. truncatula* A17 and R108 (WT sibling and *ann1-3*) were grown for 3 days on nitrogen-free paper/Fahraeus Kalys HP696 agar plates[46] before roots were spot or flood-inoculated with water (control) or a *Sm*2011-LacZ (OD_{600nm} 0.01) suspension, as described in[29]. For expression analyses of *pMtAnn1:GUS* (in pLP100) in A17 and *nin* (co-expressing or not *pEXPA:NIN*), kanamycin-resistant and/or Ds-Red fluorescence-positive composite plants were transferred 3 weeks after *A. rhizogenes* transformation to the same nitrogen-free paper/Fahraeus Kalys HP696 agar plates and grown for 3 days prior to flood inoculation (for 1h) of the entire root system with *Sm*2011-LacZ (OD_{600nm} 0.01). Plants grown *in vitro* on plates were all cultivated at 25°C under a 16-h photoperiod and a light intensity of 70 mE/s/m^2 with their root systems protected from light by wrapping ¾ of the plates with dark plastic bags.

For phenotyping experiments, germinated seedlings of *M. truncatula* R108 lines (R108, WT sibling and *ann1-1 to ann1-3* mutants), and selected composite plants (2-3 weeks after transformation) of A17-transformed with MtAnn1-RNAi/control constructs or R108 (WT or *ann1-3*)-transformed with *p35S:GFP/p35S:MtAnn1-GFP* constructs, were transferred to 8 x 8 x 7cm pots (3 plants/pot for germinated seedlings and 2 plants/pot for composite plants) filled with inert attapulgite substrate (Oil Dri US Special; http://www.oildri.com/), supplemented with 10mL nitrogen-free Fahraeus medium. For longer growth periods (> 3 wpi), plants were grown in 9 x 9 x 8 cm pots (3 plants/pot) supplemented with 14mL medium. Pots were placed in small greenhouses at 25°C, with a 16 h photoperiod and a light intensity of 100 mE/s/m^2,

and inoculated with a suspension of *Sm*2011-LacZ (OD_{600nm} 0.1), after 3 days of nitrogen starvation.

To assess mycorrhizal root colonization of WT and *ann1-3* mutant lines, germinated seedlings were transferred to 8 x 8 x 7cm pots (1 plant per pot), filled with a 1:1 mix of Zeolite substrate fractions 1.0-2.5 mm and 0.5-1.0 mm (Symbiom LTD, Lanskroun, Czech Republic), and inoculated with *R. irregularis* spores (strain DAOM197198, 150 spores per pot). Pots were placed in 60 x 40 x 12 cm trays in a 16 h photoperiod chamber (light intensity: 300 µmol m^{-2} s^{-1}) at a day-time temperature of 22 °C day and a night-time temperature of 20°C and 70% humidity. Plants were watered weekly with a modified low-phosphate and low-nitrogen Long Ashton solution (7.5 µM Na_2HPO_4, 750 µM KNO_3, 400 µM $Ca(NO_3)_2$, 200 mg/L MES buffer, pH 6.5).

β-glucuronidase (GUS) and β-galactosidase enzymatic assays

Root segments from *M. truncatula* composite plants expressing *pMtAnn1:GUS* (in pLP100) or *pEXPA:NIN + pMtAnn1:GUS* constructs were collected from control (water) or rhizobia-inoculated roots and incubated in 0.5 % paraformaldehyde/0.1 M potassium phosphate buffer pH 7.0, for 1 h, prior to histochemical (blue) staining for GUS activity for 2-5 hours at 37 °C using 1 mM of the substrate X-Gluc (5-bromo-4-chloro-3-indoxyl-b-D-GlcA, cyclohexylammonium salt, B7300; Biosynth, Staad, Switzerland) as described[48]. For mycorrhizal roots expressing *pMtAnn1:GUS*, composite plants were harvested 4 weeks after inoculation with *R. irregularis*. The root system was vacuum-infiltrated five times for 5 min each with GUS staining solution (0.5 mg/ml X-Gluc, 100 mM phosphate buffer pH 7.0, 100 mM EDTA, 0.5 mM $K_4[Fe(CN)_6]$, 0.5 mM $K_3[Fe(CN)_6]$ and 0.1% Triton X-100), and then incubated in this solution for 1 h at 37 °C in the dark. Histochemical GUS staining of *N. benthamiana* leaf discs was carried out in the same X-Gluc substrate but supplemented with 0,1 % triton, first under vacuum for 20 min at room temperature before incubation at 37 °C for 3 h. Enzymatic GUS fluorimetric assays of *N. benthamiana* leaf discs were done according to [46]. Briefly, tissues were ground using a MM400 grinder (Retsch) and homogenized in GUS extraction buffer before 1 µg of total protein extracts were used for enzymatic reactions at 37°C using 1 mM of the 4-MUG substrate (4-Methylumbelliferyl-β-D-glucuronide hydrate, Biosynth M-5700). GUS activity was measured using a FLUOstar Omega 96 microplate reader (BMG LABTECH, France) through quantification of the fluorescence of 4-MU (4-Methylumbelliferone, Sigma) reaction product. To reveal the constitutive β-galactosidase activity of the *S. meliloti* strain *Sm2011-lacZ* in ITs, root samples (sometimes pre-stained for GUS activity) were rinsed and fixed for 1 h in 1.25 % glutaraldehyde/Z buffer (10 mM KCl, 1 mM $MgCl_2$, and 0.1 M phosphate buffer, pH 7.0) as described[46]. After rinsing in Z-buffer, root samples were incubated overnight in the dark at 28 °C in Z-buffer containing 2 mM Magenta-Gal (5-bromo-6-chloro-3-indoxyl-b-D-galactopyranoside; B7200; Biosynth) or X-Gal (5-bromo-4-chloro-3-indolyl-b-D-galactopyranoside, W5376C; Thermo Fisher Scientific, Guilford, CT). GUS and/or LacZ-stained tissues were cleared for 30 s with 12 % sodium hypochlorite solution before microscopy observations.

Tissue harvesting and microscopy methods

Roots of *M. truncatula* composite plants expressing different fluorescent fusions and grown under LUMOX film were observed using a Leica TCS SP8 AOBS laser scanning confocal microscope equipped with a 40x long distance water immersion objective (HCX APO L U-V-I 40x/0.80 WATER). Confocal images were recorded using Leica LAS-X software, before and after rhizobia inoculation (from 1 to 7 dpi). For GFP, CFP and Ds-Red fluorescent proteins, 458 nm and 488 nm Argon laser lines and a 561 nm diode were used for excitation, respectively, with emission windows set at 465-495 nm, 500-525 nm and 570-600 nm (hybrid detector), respectively. To avoid potential interference, sequential mode was used to acquire CFP and red fluorescent protein fluorescence separately from GFP fluorescence and bright-field images. For confocal imaging of calcium responses, the 561 nm diode was used to excite the mApple red fluorescent protein from the NR-GECO1 sensor, and the emitted fluorescence was recovered using a hybrid detector in the 600 to 643 nm emission window. Time series (t-series) were acquired at 5 s intervals for 10 to 15 min, with pinhole diameter set to 3 Airy units, as described[44].

Roots or nodulated roots of *M. truncatula* A17 and R108 (WT and *ann1-3*) or composite plants were selected on the basis of their fluorescence and/or analyzed before or after GUS and/or β-galactosidase staining using stereomicroscopy (Leica S6E) or light microscope (AxioPlan II Imaging; Carl Zeiss, Oberkochen, Germany). For *pMtAnn1:GUS* (in pLP100) expression analysis, samples were harvested 0 and 4 dpi with rhizobia. For comparative phenotyping of wild-type and *MtAnn1* mutant or RNAi roots, β-galactosidase stained nodulated root samples were harvested 4, 5, 7, 8, 10 or 11 dpi with rhizobia. To quantify nodule size (Fig. 5E) and rhizobia infection levels (Fig. 6K), β-galactosidase-stained nodulated root systems (10 dpi) from WT and *ann1-3* plants were scanned (Objectscan 1600, Microtek) and the acquired images (TIFF) were used for image quantification.

For high-resolution microscopy analyses of pre-infection priming responses in A17, control roots and rhizobia-infected root regions or nodule primordia were carefully isolated 5-6 dpi in fixative solution from spot-inoculated or flood-inoculated root systems (after histochemical revelation of rhizobial β-galactosidase activity). Harvested root sections or nodule primordia were fixed in 2% glutaraldehyde, diluted in 0.2 M cacodylate buffer pH=7.3 for a few hours at room temperature or 1-3 days at 4°C, then rinsed with buffer, before progressive dehydration in an ethanol series and final inclusion in LR White resin following manufacturer's instructions (EMS). For comparative ultrastructural analysis of isolated WT and *ann1-3* nodules, nodule samples were carefully isolated from rhizobia-inoculated root systems 14-16 dpi and fixed under vacuum in 2 successive batches of 2.5% glutaraldehyde diluted in 0.2 M cacodylate buffer pH=7.3, the first batch containing saponin or triton (0.1 % final) for 3-5 days at 4°C. After rinsing in buffer, post-fixation in 2% osmium tetroxyde (diluted in 0.2 M sodium cacodylate), rinsing again in buffer, progressive dehydration in an ethanol series and incubation in propylene oxide (2 x 1h), samples were finally embedded in Epon 812 resin (EMS) following the manufacturer's instructions. For all samples, semi-thin (1 µm) and ultra-thin (80 nm) sections were generated using an Ultracut E ultramicrotome (Reichert Jung). Semi-thin sections of root/nodule primordia (5-6 dpi) were stained with basic fuchsin (0.07 % in water) to help visualize ITs, while mature nodule sections (14-16 dpi) were stained in an aqueous solution with methylene blue (0.2 %), toluidine blue (1 %), borax (1 %) and basic fuchsin (0.07 %) before observation by bright field microscopy (Axioplan II Imaging; Carl Zeiss). Ultrathin sections (80 nm) were contrasted with Uranyless and lead citrate (Delta microscopy) and observed using a Hitachi 7700 electron microscope (Hitachi High-Tech).

For histochemical GUS staining of mycorrhizal roots, selected composite plants transformed with *pMtAnn1:GUS* were transferred to 7 x 7 x 8 cm pots (5 plants/pot) filled with washed quartz sand (grain size 0.7-1.2 mm) pre-watered with modified half-strength Hoagland solution containing 20 µM phosphate[79]. Each plant was inoculated with 500 spores of *R. irregularis* DAOM197198 (C-grade, Agronutrition, Toulouse, France). Plants were grown in a Polyklima cabinet at 22°C constant temperature, 60 % air humidity and 16-h-light/8-h-dark cycles, at 200 µE m−2 s−1 light intensity and a combination of warm and cold LED 'True DayLight' at a 40:25 ratio. Pots were watered twice per week with 30-40 ml of autoclaved de-ionized tap water, and fertilized once per week with 30-40 ml of modified half-strength Hoagland solution containing 20 µM phosphate. To visualize the fungal structures, the GUS staining solution was exchanged for 10 % KOH and the roots incubated for 15 min at 95°C. After KOH removal, the roots were washed 3 times with de-ionized water. After addition of 0.1 M HCl, the roots were further incubated for 2 h in the dark at room temperature. HCl was removed and the roots were washed 3 times with de-ionized water and once with PBS. This was followed by an overnight incubation at room temperature in the dark with 200 ng/µL WGA Alexa Fluor 488 (Invitrogen W11261) in PBS. Roots were imaged with a LEICA DM6B epifluorescence microscope. To compare the extent of mycorrhizal colonization of roots between WT and *ann1-3* lines, whole root systems were collected 6 weeks post-inoculation with *R. irregularis* and cleared by boiling (95°C) in 10% KOH for 5 minutes, rinsed with water, then stained by boiling in an acidic ink solution (5% acetic acid, 5% Sheaffer black ink #94321, in water) to reveal fungal structures. Overall intraradical colonization rates and arbuscular density were estimated in ink-stained roots under a stereomicroscope (Leica S6E) using the gridline intersect method.

Microscopy image analyses

Analysis of confocal t-series was performed using the Fiji software[80]. Intensity data were calculated from selected regions of interest (ROIs), corresponding to single nuclei, imaged in independent roots, in 2-3 independent experiments. Maximal z-projections of stacks and merged confocal images were prepared using Leica confocal software or Fiji. To quantify relative amplitudes of Ca^{2+} spiking, the mean fluorescence of each ROI was measured as a function of time and used to determine the Signal-to-Noise Ratio (SNR). The SNR measures the difference between the fluorescence at each time-point (F_t) and the fluorescence baseline, calculated as the average of 4 fluorescence values taken 10 and 15 sec before and after t (F_{t-3}; F_{t-2}; F_{t2+}; F_{t+3}). A threshold of 0.3 was applied to the SNR to define individual peaks, and the amplitude of Ca^{2+} spiking was calculated for each nucleus as the mean peak SNR value. Spiking frequency, defined as the number of peaks observed in 10 min, was also calculated.

Scanned images of β-galactosidase-stained nodules from R108* and *ann1-3* (10 dpi) were imported to Ilastik software[81] to enable machine-learning recognition of blue β-galactosidase-stained nodules (pixel-based classification method). Objects identified as nodules were exported in a new single segmentation .tiff file for analysis in ImageJ to measure specific nodule features (length, size and infection level, based on the blue intensity of rhizobial β-galactosidase activity).

Transient expression assays in *N. benthamiana* leaves

An *A. tumefaciens* GV3101 strain carrying the *pMtAnn1:GUS* fusion construct (in pLP100) was used for infiltration studies in *N. benthamiana* alone or with *A. tumefaciens* GV3103 strains carrying *p35S:NIN* or *p35S:NINΔ* constructs[52], designed to constitutively express NIN or NINΔ under the 35S promoter in transactivation experiments. Briefly, *A. tumefaciens* strains grown overnight at 28°C in Luria-Bertani with appropriate antibiotics were harvested and resuspended in Agromix (10 mM $MgCl_2$, 10 mM MES/KOH pH 5.6 and Acetosyringone in DMSO Sigma-Aldrich 150 µM) and kept in the dark for at least 2h, at room temperature. Equal volumes of *A. tumefaciens* cultures (OD_{600}=0.25) were used to co-infiltrate leaf discs of 3-week-old *N. benthamiana* plants. Infiltrated plants were kept at 21°C in a growth chamber (16-h photoperiod and a light intensity of 70 mE m22 s21) for 36 h prior to histochemical GUS assays or storage at -70°C prior to protein extraction for Western-blot or fluorimetric GUS assays.

Western blot analyses

N. benthamiana leaf discs, previously stored at -80°C, were ground using a MM400 (Retsch) crusher and resuspended in Laemmli 2X sample buffer for SDS-PAGE (Bio-rad). Samples were then placed at 95°C for 3min and centrifuged at 13200 rpm for 1 min. For each sample, 10 µL of the supernatant was loaded in a polyacrylamide 4-15% Mini-PROTEAN precast gel (Bio-Rad) along with 5 µL of pre-stained protein ladder marker (ThermoScientific, Lithuania). The Mini-Protean tank Electrophoresis System (Biorad, USA) was used for gel migration in 1 X Tris/Glycine/SDS Buffer (Bio-Rad). Protein transfer to nitrocellulose membranes (Bio-Rad) was performed using a Trans-Blot Turbo semi-dry transfer system (Bio-Rad). Membranes were stained with Ponceau Red before incubation for 1 h in blocking 1 x TBS solution (Tris base, NaCl and H_2O), 0.1 % Tween, 5 % milk at room temperature, with mild agitation, before rinsing 3 x in TBS-Tween 0.1 % for 10 min, and incubated overnight in the same solution at 4°C with a 6000 X dilution of anti-HA-peroxidase antibodies (Sigma-Aldrich) in 0.5 % milk in TBS-Tween 0.1 % to reveal HA-tagged NIN proteins following chemiluminescence revelation using the Clarity Western ECL Substrate (Bio-Rad) and the ChemiDoc Touch imaging system (Bio-Rad).

Acetylene reduction assay

To assess nitrogenase activity, grouped nodules were isolated from root systems of plants grown in pots 3 weeks after inoculation with *Sm*2011-LacZ and tested for acetylene reduction. Nodules were incubated at 25°C in sealed 60 mL vials containing 0.5 mL of nitrogen-free Fahraeus liquid medium in the presence of 10 % (v/v) acetylene for 3 h. 400 µL of gaz was then collected from each vial and ethylene production was quantified by gas chromatography (model no. GC 7280A; Agilent Technologies, Lexington, MA).

RNA extraction and quantitative RT-PCR analysis

Total RNA was extracted from *M. truncatula* control and rhizobia-inoculated roots (4-5 dpi) using the Macherey-Nagel total RNA isolation kit according to the manufacturer's instructions. DNA-free RNA samples were quantified and RNA integrity was verified by Agilent RNA Nano Chip (Agilent Technologies). First-strand complementary DNA synthesis was performed using 1 µg of total RNA using an anchored oligo (dT) and Transcriptor Reverse Transcriptase (Roche) following the manufacturers' protocol. Quantitative RT-PCR was performed on 384-well plates, with the Light Cycler 480 system (Roche) and using the SYBR Green I Master mix

(Roche), according to the manufacturer's instructions. Reactions and cycling conditions were performed as described before[29] using Primer pairs listed in Supplementary Table S1. The specificity of the PCR amplification was verified by analysing the PCR dissociation curve and sequencing of the PCR product. Transcript levels were normalized to the endogenous Ubiquitin reference.

Phylogenetic analysis

Protein sequence of *MtAnn1* (MtrunA17_Chr8g0352611) was used as query to search against a database containing 227 plant genomes covering the main lineages of green plants and five SAR genomes as outgroups using the BLASTp v2.14.0+ with an e-value threshold of 1e-10[55]. Homologous proteins were then aligned using Muscle v5.1 with the "super5" option[82] and trimmed to remove positions with more than 60% of gaps using trimAl v1.4.rev22[83]. The trimmed alignment served as matrix for phylogenetic reconstruction using FastTree v2.1.11-OpenMP[84]. To gain insights about the evolution of Ann1 in relation with the nitrogen-fixing symbiosis, the flowering clade corresponding containing orthologs of MtAnn1 has been extracted and proteins re-aligned using Muscle with default parameters before trimming as described above. Few spurious sequences with obvious mispositioning and abnormal short sequences were removed. Then, maximum likelihood tree has been reconstructed using IQ-TREE v2.1.2[85] after testing the best evolution model using ModelFinder[86] as implemented in IQ-TREE2 and according to the Bayesian Information Criteria. Branch supports have been tested with 10,000 replicates of both SH-aLRT[87] and UltraFast Bootstraps with UFBoot2[88]. Finally, trees were visualized and annotated in the iTOL platform v6.8.1[89].

Graph generation and Statistical Analyses

Graph preparation and statistical analyses were performed using R (http://r-project. org), with the exception of data in Fig. 6J, which was generated using Microsoft Excel and for which statistical contingency analysis was performed using GraphPad Prism 10. Normal distribution of the data was evaluated using the Shapiro-Wilk test, and homogeneity of variance was assessed using Fisher or Bartlett tests. Parametric statistical tests (t-test, ANOVA) were used to analyze data with a normal distribution, while the non-parametric Mann-Whitney statistical test was used for data with a non-normal distribution. When applicable, a transformation was performed to normalize data distribution (Log10 or BoxCox). Number of individually analyzed samples (n), replicates and *p* significance levels are indicated in Figure legends. In details, data were analyzed as follows: values in Fig. 2E follow a normal distribution and display homogeneous variance, so a two-tailed Student t-test was performed (t=-3.0927, df=39, p=0.0037). Values in Fig. 2F do not follow a normal distribution and were thus analyzed using a two-tailed Mann-Whitney test (W=315, p=0.1531). Log10-transformed values in Fig. 4E follow a normal distribution and variance homogeneity and were thus analyzed using one-way ANOVA followed by Tukey honest significant difference (HSD) tests (F=149.5, df=2, p<2e-16). Values in Fig. 5D follow a normal distribution and variance homogeneity and were thus analyzed using a two-tailed Student t-test (t=-3.51, df=89, p=0.0007). Values in Fig. 5E display a non-normal distribution and were thus analyzed using a two-tailed Mann-Whitney test (W=163255, p=1.26e-07). Log10-transformed values in Fig. 5F show a normal distribution and variance homogeneity, and were thus analyzed using a two-tailed Student t-test (t=-3.066,

df=27, p=0.0049). Values in Fig. 6A-C, do not follow a normal distribution, they were thus analyzed using two-tailed Mann-Whitney tests (6A: W=1189.5, p=0.0487; 6B: W=1207.5, p=0.0332; 6C: W=1233.5, p=0.0182). For Fig. 6J, a chi-square test was performed on a contingency table reporting the number of cortically-extended ITs per individual NP for WT and *ann1-3* plants (χ_2=15.35, df=2, p=0.0005). Values in Fig. 6K with a non-normal distribution were analyzed using a two-tailed Mann-Whitney test (W=180905, p=2.2e-16). Values in Fig. 7A-B, which show a normal distribution and variance homogeneity were analyzed using one-tailed Student t-tests, due to the low number of values (7A: t=2.1821, df=9, p=0.0285; 7B: t=0.9612, df=22, p=0.1735). In Fig. 7C, values do not follow a normal distribution, thus a two-tailed Mann-Whitney test was performed (W=9944, p=0.0018). In Fig. 8, values in 8A and BoxCox-transformed values in 8B (λ=1.353535) show a normal distribution and homogeneity of variance and were thus analyzed using two-tailed Student t-test (8A: t=3.6816, df=72, p=0.0004448; 8B: t=3.8831, df=72, p=0.0002265). In Supplementary Fig. S1E-F, values show a non-normal distribution and were thus analyzed using two-tailed Mann-Whitney tests (S1E: W=853, p=1.811e-07; S1F: W=205, p=2.893e-05). In Supplementary Fig. S4B-C, BoxCox-transformed S4B values (λ= 0.1010101) and Log10-transformed S4C values follow a normal distribution and homogeneity of variance and were thus analyzed using one-way ANOVA followed by Tukey honest significant difference (HSD) tests (S4B: F=681.2, df=4, p<2e-16 ; S4C: F=2.4, df=3, p=0.0783). In Supplementary Fig. S6E-G, values follow a normal distribution and variance homogeneity in S6E, hence a two-tailed Student t-test was carried out (t=2.4153, df=99, p=0.0176), while values in S6F-G do not follow a normal distribution, thus two-tailed Mann-Whitney tests were applied (S6F: W=1724, p=0.0023; S6G: W=1473.5, p=0.1759). In Supplementary Fig. S7C-E, values do not follow a normal distribution in S7C and E and were thus analyzed using two-tailed Mann-Whitney tests (S7C: W=18215, p=0.3726; S7E: W=86, p=0.57), which values in S7D follow a normal distribution and variance homogeneity, so values were analyzed using a two-tailed Student t-test (t=-1.0271, df=10, p=0.3286).

Data availability

The authors declare that all data supporting the results of this study are available within the article and its Supplementary Information Files. Materials generated in this study are available from the corresponding authors upon request.

References

1 Lanfranco, L., Fiorilli, V. & Gutjahr, C. Partner communication and role of nutrients in the arbuscular mycorrhizal symbiosis. *New Phytol* **220**, 1031-1046 (2018). https://doi.org/10.1111/nph.15230

2 Huisman, R. & Geurts, R. A Roadmap toward Engineered Nitrogen-Fixing Nodule Symbiosis. *Plant Commun* **1**, 100019 (2020). https://doi.org/10.1016/j.xplc.2019.100019

3 Griesmann, M. *et al.* Phylogenomics reveals multiple losses of nitrogen-fixing root nodule symbiosis. *Science* **361** (2018). https://doi.org/10.1126/science.aat1743

4 Libourel, C. *et al.* Comparative phylotranscriptomics reveals ancestral and derived root nodule symbiosis programmes. *Nat Plants* **9**, 1067-1080 (2023). https://doi.org/10.1038/s41477-023-01441-w

5 Charpentier, M. Calcium Signals in the Plant Nucleus: Origin and Function. *J Exp Bot* (2018). https://doi.org/10.1093/jxb/ery160

6 Genre, A. & Russo, G. Does a Common Pathway Transduce Symbiotic Signals in Plant-Microbe Interactions? *Front Plant Sci* **7**, 96 (2016). https://doi.org/10.3389/fpls.2016.00096

7 Krönauer, C. & Radutoiu, S. Understanding Nod factor signalling paves the way for targeted engineering in legumes and non-legumes. *Curr Opin Plant Biol* **62**, 102026 (2021). https://doi.org/10.1016/j.pbi.2021.102026

8 Lévy, J. *et al.* A putative Ca2+ and calmodulin-dependent protein kinase required for bacterial and fungal symbioses. *Science* **303**, 1361-1364 (2004). https://doi.org/10.1126/science.1093038

9 Tirichine, L. *et al.* Deregulation of a Ca2+/calmodulin-dependent kinase leads to spontaneous nodule development. *Nature* **441**, 1153-1156 (2006). https://doi.org/10.1038/nature04862

10 Singh, S., Katzer, K., Lambert, J., Cerri, M. & Parniske, M. CYCLOPS, a DNA-binding transcriptional activator, orchestrates symbiotic root nodule development. *Cell Host Microbe* **15**, 139-152 (2014). https://doi.org/10.1016/j.chom.2014.01.011

11 Cerri, M. R. *et al.* The ERN 1 transcription factor gene is a target of the CC a MK/CYCLOPS complex and controls rhizobial infection in Lotus japonicus. *New Phytologist* **215**, 323-337 (2017).

12 Pimprikar, P. & Gutjahr, C. Transcriptional Regulation of Arbuscular Mycorrhiza Development. *Plant and Cell Physiology* **59**, 678-695 (2018). https://doi.org/10.1093/pcp/pcy024

13 De Carvalho-Niebel, F., Timmers, A. C., Chabaud, M., Defaux-Petras, A. & Barker, D. G. The Nod factor-elicited annexin MtAnn1 is preferentially localised at the nuclear periphery in symbiotically activated root tissues of Medicago truncatula. *Plant J* **32**, 343-352 (2002).

14 Manthey, K. *et al.* Transcriptome profiling in root nodules and arbuscular mycorrhiza identifies a collection of novel genes induced during Medicago truncatula root endosymbioses. *Mol Plant Microbe Interact* **17**, 1063-1077 (2004). https://doi.org/10.1094/MPMI.2004.17.10.1063

15 Davies, J. M. Annexin-Mediated Calcium Signalling in Plants. *Plants (Basel)* **3**, 128-140 (2014). https://doi.org/10.3390/plants3010128

16 Kodavali, P. K. *et al.* Structural and functional characterization of annexin 1 from Medicago truncatula. *Plant Physiol Biochem* **73**, 56-62 (2013). https://doi.org/10.1016/j.plaphy.2013.08.010

17 Malabarba, J. *et al.* ANNEXIN1 mediates calcium-dependent systemic defense in Arabidopsis plants upon herbivory and wounding. *New Phytol* **231**, 243-254 (2021). https://doi.org/10.1111/nph.17277

18 Liao, C., Zheng, Y. & Guo, Y. MYB30 transcription factor regulates oxidative and heat stress responses through ANNEXIN-mediated cytosolic calcium signaling in Arabidopsis. *New Phytol* **216**, 163-177 (2017). https://doi.org/10.1111/nph.14679

19 Richards, S. L. *et al.* Annexin 1 regulates the H2O2-induced calcium signature in Arabidopsis thaliana roots. *Plant J* **77**, 136-145 (2014). https://doi.org/10.1111/tpj.12372

20 Gutjahr, C. & Parniske, M. Cell and developmental biology of arbuscular mycorrhiza symbiosis. *Annu Rev Cell Dev Biol* **29**, 593-617 (2013). https://doi.org/10.1146/annurev-cellbio-101512-122413

21 Gage, D. J. Infection and invasion of roots by symbiotic, nitrogen-fixing rhizobia during nodulation of temperate legumes. *Microbiol Mol Biol Rev* **68**, 280-300 (2004). https://doi.org/10.1128/MMBR.68.2.280-300.2004

22 Roth, R. *et al.* Arbuscular cell invasion coincides with extracellular vesicles and membrane tubules. *Nat Plants* **5**, 204-211 (2019). https://doi.org/10.1038/s41477-019-0365-4

23 Ivanov, S., Austin, J., Berg, R. H. & Harrison, M. J. Extensive membrane systems at the host-arbuscular mycorrhizal fungus interface. *Nat Plants* **5**, 194-203 (2019). https://doi.org/10.1038/s41477-019-0364-5

24 Fournier, J. *et al.* Remodeling of the infection chamber before infection thread formation reveals a two-step mechanism for rhizobial entry into the host legume root hair. *Plant physiology* **167**, 1233--1242 (2015). https://doi.org/10.1104/pp.114.253302

25 Liang, P. *et al.* Formin-mediated bridging of cell wall, plasma membrane, and cytoskeleton in symbiotic infections of Medicago truncatula. *Curr Biol* **31**, 2712-2719.e2715 (2021). https://doi.org/10.1016/j.cub.2021.04.002

26 Su, C. *et al.* Transcellular progression of infection threads in Medicago truncatula roots is associated with locally confined cell wall modifications. *Curr Biol* **33**, 533-542.e535 (2023). https://doi.org/10.1016/j.cub.2022.12.051

27 Liu, C. W. *et al.* A protein complex required for polar growth of rhizobial infection threads. *Nat Commun* **10**, 2848 (2019). https://doi.org/10.1038/s41467-019-10029-y

28 Lace, B. *et al.* RPG acts as a central determinant for infectosome formation and cellular polarization during intracellular rhizobial infections. *Elife* **12** (2023). https://doi.org/10.7554/eLife.80741

29 Gaudioso-Pedraza, R. *et al.* Callose-Regulated Symplastic Communication Coordinates Symbiotic Root Nodule Development. *Curr Biol* **28**, 3562-3577.e3566 (2018). https://doi.org/10.1016/j.cub.2018.09.031

30 Xiao, T. T. *et al.* Fate map of Medicago truncatula root nodules. *Development* **141**, 3517-3528 (2014). https://doi.org/10.1242/dev.110775

31 Lin, J., Frank, M. & Reid, D. No Home without Hormones: How Plant Hormones Control Legume Nodule Organogenesis. *Plant Commun* **1**, 100104 (2020). https://doi.org/10.1016/j.xplc.2020.100104

32 Chaulagain, D. & Frugoli, J. The Regulation of Nodule Number in Legumes Is a Balance of Three Signal Transduction Pathways. *Int J Mol Sci* **22** (2021). https://doi.org/10.3390/ijms22031117

33 Genre, A., Chabaud, M., Faccio, A., Barker, D. G. & Bonfante, P. Prepenetration apparatus assembly precedes and predicts the colonization patterns of arbuscular mycorrhizal fungi within the root cortex of both Medicago truncatula and Daucus carota. *Plant Cell* **20**, 1407-1420 (2008). https://doi.org/10.1105/tpc.108.059014

34 Van Brussel, A. A. N. *et al*. Induction of pre-infection thread structures in the leguminous host plant by mitogenic lipo-oligosaccharides of Rhizobium. *Science* **257**, 70-72 (1992).

35 Genre, A., Ortu, G., Bertoldo, C., Martino, E. & Bonfante, P. Biotic and abiotic stimulation of root epidermal cells reveals common and specific responses to arbuscular mycorrhizal fungi. *Plant Physiol* **149**, 1424-1434 (2009). https://doi.org/10.1104/pp.108.132225

36 Russo, G. & Genre, A. Divide and Be Conquered-Cell Cycle Reactivation in Arbuscular Mycorrhizal Symbiosis. *Front Plant Sci* **12**, 753265 (2021). https://doi.org/10.3389/fpls.2021.753265

37 Batzenschlager, M., Lace, B., Zhang N, Su, C., Egli, S., Krohn, P., Salfeld, J., D. F. A., Laux, T., Ott, T. Competence for transcellular infection in the root cortex involves a post-replicative, cell-cycle exit decision in Medicago truncatula. bioRxiv (2023).

38 Perrine-Walker, F. M., Lartaud, M., Kouchi, H. & Ridge, R. W. Microtubule array formation during root hair infection thread initiation and elongation in the Mesorhizobium-Lotus symbiosis. *Protoplasma* **251**, 1099-1111 (2014). https://doi.org/10.1007/s00709-014-0618-z

39 Yang, W. C. *et al.* Rhizobium nod factors reactivate the cell cycle during infection and nodule primordium formation, but the cycle is only completed in primordium formation. *Plant Cell* **6**, 1415-1426 (1994). https://doi.org/10.1105/tpc.6.10.1415

40 Timmers, A. C., Auriac, M. C. & Truchet, G. Refined analysis of early symbiotic steps of the Rhizobium-Medicago interaction in relationship with microtubular cytoskeleton rearrangements. *Development* **126**, 3617-3628 (1999).

41 Fournier, J. *et al.* Mechanism of infection thread elongation in root hairs of Medicago truncatula and dynamic interplay with associated rhizobial colonization. *Plant Physiol* **148**, 1985-1995 (2008). https://doi.org/10.1104/pp.108.125674

42 Sieberer, B. J., Chabaud, M., Fournier, J., Timmers, A. C. & Barker, D. G. A switch in Ca2+ spiking signature is concomitant with endosymbiotic microbe entry into cortical root cells of Medicago truncatula. *Plant J* **69**, 822-830 (2012). https://doi.org/10.1111/j.1365-313X.2011.04834.x

43 Takeda, N., Maekawa, T. & Hayashi, M. Nuclear-localized and deregulated calcium- and calmodulin-dependent protein kinase activates rhizobial and mycorrhizal responses in Lotus japonicus. *Plant Cell* **24**, 810-822 (2012). https://doi.org/10.1105/tpc.111.091827

44 Kelner, A., Leitão, N., Chabaud, M., Charpentier, M. & de Carvalho-Niebel, F. Dual Color Sensors for Simultaneous Analysis of Calcium Signal Dynamics in the Nuclear and Cytoplasmic Compartments of Plant Cells. *Front Plant Sci* **9**, 245 (2018). https://doi.org/10.3389/fpls.2018.00245

45 Schnabel, E., Journet, E. P., de Carvalho-Niebel, F., Duc, G. & Frugoli, J. The Medicago truncatula SUNN gene encodes a CLV1-like leucine-rich repeat receptor kinase that regulates nodule number and root length. *Plant Mol Biol* **58**, 809-822 (2005). https://doi.org/10.1007/s11103-005-8102-y

46 Cerri, M. R. *et al.* Medicago truncatula ERN transcription factors: regulatory interplay with NSP1/NSP2 GRAS factors and expression dynamics throughout rhizobial infection. *Plant Physiol* **160**, 2155-2172 (2012). https://doi.org/10.1104/pp.112.203190

47 Middleton, P. H. *et al.* An ERF transcription factor in Medicago truncatula that is essential for Nod factor signal transduction. *Plant Cell* **19**, 1221-1234 (2007). https://doi.org/10.1105/tpc.106.048264

48 Cerri, M. R. *et al.* The Symbiosis-Related ERN Transcription Factors Act in Concert to Coordinate Rhizobial Host Root Infection. *Plant Physiol* **171**, 1037-1054 (2016). https://doi.org/10.1104/pp.16.00230

49 Wais, R. J. *et al.* Genetic analysis of calcium spiking responses in nodulation mutants of Medicago truncatula. *Proc Natl Acad Sci U S A* **97**, 13407-13412 (2000). https://doi.org/10.1073/pnas.230439797

50 Rival, P. *et al.* Epidermal and cortical roles of NFP and DMI3 in coordinating early steps of nodulation in Medicago truncatula. *Development* **139**, 3383-3391 (2012). https://doi.org/10.1242/dev.081620

51 Schiessl, K. *et al.* NODULE INCEPTION Recruits the Lateral Root Developmental Program for Symbiotic Nodule Organogenesis in Medicago truncatula. *Curr Biol* **29**, 3657-3668.e3655 (2019). https://doi.org/10.1016/j.cub.2019.09.005

52 Vernie, T. *et al.* The NIN Transcription Factor Coordinates Diverse Nodulation Programs in Different Tissues of the Medicago truncatula Root. *Plant Cell* **27**, 3410-3424 (2015). https://doi.org/10.1105/tpc.15.00461

53 Liu, H. *et al.* A genetic screen for plant mutants with altered nodulation phenotypes in response to rhizobial glycan mutants. *New Phytol* **220**, 526-538 (2018). https://doi.org/10.1111/nph.15293

54 Vasse, J., de Billy, F., Camut, S. & Truchet, G. Correlation between ultrastructural differentiation of bacteroids and nitrogen fixation in alfalfa nodules. *J Bacteriol* **172**, 4295-4306 (1990). https://doi.org/10.1128/jb.172.8.4295-4306.1990

55 Radhakrishnan, G. V. *et al.* An ancestral signalling pathway is conserved in intracellular symbioses-forming plant lineages. *Nat Plants* **6**, 280-289 (2020). https://doi.org/10.1038/s41477-020-0613-7

56 Clark, G. B., Morgan, R. O., Fernandez, M. P. & Roux, S. J. Evolutionary adaptation of plant annexins has diversified their molecular structures, interactions and functional roles. *New Phytol* **196**, 695-712 (2012). https://doi.org/10.1111/j.1469-8137.2012.04308.x

57 Seguí-Simarro, J. M., Coronado, M. J. & Staehelin, L. A. The mitochondrial cycle of Arabidopsis shoot apical meristem and leaf primordium meristematic cells is defined by a perinuclear tentaculate/cage-like mitochondrion. *Plant Physiol* **148**, 1380-1393 (2008). https://doi.org/10.1104/pp.108.126953

58 Costa, A., Navazio, L. & Szabo, I. The contribution of organelles to plant intracellular Calcium signalling. *J Exp Bot* (2018). https://doi.org/10.1093/jxb/ery185

59 Cui, Y. *et al.* A whole-cell electron tomography model of vacuole biogenesis in Arabidopsis root cells. *Nat Plants* **5**, 95-105 (2019). https://doi.org/10.1038/s41477-018-0328-1

60 Genre, A. *et al.* Multiple exocytotic markers accumulate at the sites of perifungal membrane biogenesis in arbuscular mycorrhizas. *Plant Cell Physiol* **53**, 244-255 (2012). https://doi.org/10.1093/pcp/pcr170

61 Viotti, C. ER and vacuoles: never been closer. *Front Plant Sci* **5**, 20 (2014). https://doi.org/10.3389/fpls.2014.00020

62 Evans, R. C. & Blackwell, K. T. Calcium: amplitude, duration, or location? *Biol Bull* **228**, 75-83 (2015). https://doi.org/10.1086/BBLv228n1p75

63 Whalley, H. J. & Knight, M. R. Calcium signatures are decoded by plants to give specific gene responses. *New Phytol* **197**, 690-693 (2013). https://doi.org/10.1111/nph.12087

64 Xu, T., Niu, J. & Jiang, Z. Sensing Mechanisms: Calcium Signaling Mediated Abiotic Stress in Plants. *Front Plant Sci* **13**, 925863 (2022). https://doi.org/10.3389/fpls.2022.925863

65 Del Cerro, P. *et al.* Engineered CaM2 modulates nuclear calcium oscillation and enhances legume root nodule symbiosis. *Proc Natl Acad Sci U S A* **119**, e2200099119 (2022). https://doi.org/10.1073/pnas.2200099119

66 Laohavisit, A. *et al.* Arabidopsis annexin1 mediates the radical-activated plasma membrane Ca^{2}+- and K+-permeable conductance in root cells. *Plant Cell* **24**, 1522-1533 (2012). https://doi.org/10.1105/tpc.112.097881

67 Tichá, M. *et al.* Advanced Microscopy Reveals Complex Developmental and Subcellular Localization Patterns of ANNEXIN 1 in. *Front Plant Sci* **11**, 1153 (2020). https://doi.org/10.3389/fpls.2020.01153

68 Zhao, Z. X. *et al.* ANNEXIN 8 negatively regulates RPW8.1-mediated cell death and disease resistance in Arabidopsis. *J Integr Plant Biol* **63**, 378-392 (2021). https://doi.org/10.1111/jipb.13025

69 Vais, H. *et al.* ER-luminal [Ca2+] regulation of InsP3 receptor gating mediated by an ER-luminal peripheral Ca2+-binding protein. *Elife* **9** (2020). https://doi.org/10.7554/eLife.53531

70 Peiter, E. The plant vacuole: emitter and receiver of calcium signals. *Cell Calcium* **50**, 120-128 (2011). https://doi.org/10.1016/j.ceca.2011.02.002

71 Himschoot, E., Pleskot, R., Van Damme, D. & Vanneste, S. The ins and outs of Ca. *Curr Opin Plant Biol* **40**, 131-137 (2017). https://doi.org/10.1016/j.pbi.2017.09.003

72 Ruan, H., Wang, T., Ren, H. & Zhang, Y. AtFH5-labeled secretory vesicles-dependent calcium oscillation drives exocytosis and stepwise bulge during pollen germination. *Cell Rep* **42**, 113319 (2023). https://doi.org/10.1016/j.celrep.2023.113319

73 Konopka-Postupolska, D. & Clark, G. Annexins as Overlooked Regulators of Membrane Trafficking in Plant Cells. *Int J Mol Sci* **18** (2017). https://doi.org/10.3390/ijms18040863

74 Takatsuka, H., Higaki, T. & Ito, M. At the Nexus between Cytoskeleton and Vacuole: How Plant Cytoskeletons Govern the Dynamics of Large Vacuoles. *Int J Mol Sci* **24** (2023). https://doi.org/10.3390/ijms24044143

75 Lhuissier, F. G. P., De Ruijter, N. C. A., Sieberer, B. J., Esseling, J. J., Emons, A. M. C. Time Course of Cell Biological Events Evoked in Legume Root Hairs by Rhizobium Nod Factors: State of the Art. *Annals of Botany* **87**, 289-302 (2001).

76 Sieberer, B. a. E., Anne Mie C. Cytoarchitecture and pattern of cytoplasmic streaming in root hairs of Medicago truncatula during development and deformation by nodulation factors. *Protoplasma* **214**, 118-127 (2000).

77 Carrasco-Castilla, J., Ortega-Ortega, Y., Jáuregui-Zúñiga, D., Juárez-Verdayes, M. A., Arthikala, M.-K., Monroy-Morales, E., Nava, N., Santana, O., Sánchez-López, R., Quinto, C. *Environmental and Experimental Botany* **153**, 108-119 (2018).

78 Marsh, J. F. *et al.* Medicago truncatula NIN is essential for rhizobial-independent nodule organogenesis induced by autoactive calcium/calmodulin-dependent protein kinase. *Plant Physiol* **144**, 324-335 (2007). https://doi.org/10.1104/pp.106.093021

79 Zeng, T. *et al.* Host- and stage-dependent secretome of the arbuscular mycorrhizal fungus Rhizophagus irregularis. *Plant J* **94**, 411-425 (2018). https://doi.org/10.1111/tpj.13908

80 Schindelin, J. *et al.* Fiji: an open-source platform for biological-image analysis. *Nat Methods* **9**, 676-682 (2012). https://doi.org/10.1038/nmeth.2019

81 Berg, S. *et al.* ilastik: interactive machine learning for (bio)image analysis. *Nat Methods* **16**, 1226-1232 (2019). https://doi.org/10.1038/s41592-019-0582-9

82 Edgar, R. C. Muscle5: High-accuracy alignment ensembles enable unbiased assessments of sequence homology and phylogeny. *Nat Commun* **13**, 6968 (2022). https://doi.org/10.1038/s41467-022-34630-w

83 Capella-Gutiérrez, S., Silla-Martínez, J. M. & Gabaldón, T. trimAl: a tool for automated alignment trimming in large-scale phylogenetic analyses. *Bioinformatics* **25**, 1972-1973 (2009). https://doi.org/10.1093/bioinformatics/btp348

84 Price, M. N., Dehal, P. S. & Arkin, A. P. FastTree 2--approximately maximum-likelihood trees for large alignments. *PLoS One* **5**, e9490 (2010). https://doi.org/10.1371/journal.pone.0009490

85 Minh, B. Q. *et al.* IQ-TREE 2: New Models and Efficient Methods for Phylogenetic Inference in the Genomic Era. *Mol Biol Evol* **37**, 1530-1534 (2020). https://doi.org/10.1093/molbev/msaa015

86 Kalyaanamoorthy, S., Minh, B. Q., Wong, T. K. F., von Haeseler, A. & Jermiin, L. S. ModelFinder: fast model selection for accurate phylogenetic estimates. *Nat Methods* **14**, 587-589 (2017). https://doi.org/10.1038/nmeth.4285

87 Guindon, S. *et al.* New algorithms and methods to estimate maximum-likelihood phylogenies: assessing the performance of PhyML 3.0. *Syst Biol* **59**, 307-321 (2010). https://doi.org/10.1093/sysbio/syq010

88 Hoang, D. T., Chernomor, O., von Haeseler, A., Minh, B. Q. & Vinh, L. S. UFBoot2: Improving the Ultrafast Bootstrap Approximation. *Mol Biol Evol* **35**, 518-522 (2018). https://doi.org/10.1093/molbev/msx281

89 Letunic, I. & Bork, P. Interactive Tree Of Life (iTOL) v5: an online tool for phylogenetic tree display and annotation. *Nucleic Acids Res* **49**, W293-W296 (2021). https://doi.org/10.1093/nar/gkab301

Acknowledgements

We thank Celine Remblière for providing seeds of the *M. truncatula dmi3* line carrying the *pEXT:DMI3* construct. The *M. truncatula* R108 mutant plants utilized in this research project, which are jointly owned by the Centre National De La Recherche Scientifique, were obtained from Noble Research Institute, LLC and were created through research funded, in part, by grants from the National Science Foundation, NSF #DBI-0703285 and NSF #IOS-1127155. This work was supported by French National Research grants TULIP ANR-10-LABX-41, COME-IN ANR-14-CE35-0007-01 and LIVE-SWITCH ANR-19-CE20-0026-01 to FdCN and by the European Research Council (ERC) under the European Union's Horizon 2020 research and innovation program (grant No. 759731) to CG. This work also benefited from specific financial assistance from the INRAE Plant Health and Environment department (SPE). A. G. was funded by an ANR postdoctoral grant (ANR-19-CE20-0026-01), A. K. and A. D. were funded by PhD grants from the French Ministry of National Education and Research. We acknowledge the TRI-FRAIB imaging facility, member of the national infrastructure France-BioImaging supported by the French National Research Agency (ANR-10-INBS-04).

Author contributions

Rhizobial symbiosis-related experiments were designed and performed by FdCN's team members: ultrastructural microscopy (MCA), live cell imaging in various genotypes (JF, AK, AG), promoter-GUS and Q-RT-PCR studies (LF), mutant/RNAi phenotyping (AG, AD). AM symbiosis-related experiments were designed and carried out by KH (promoter-GUS) and AG and NFF (mutant analysis). AG and AL set up the machine-learning nodule phenotyping ImageJ method, JK and PMD carried out the phylogenetic studies. AG, JF, AK, MCA, LF, KH, AD, NFF and JK analysed the data with contributions from PMD, CG or FdCN. FdCN designed the research and wrote the article with AG and JF and key contributions from the other authors.

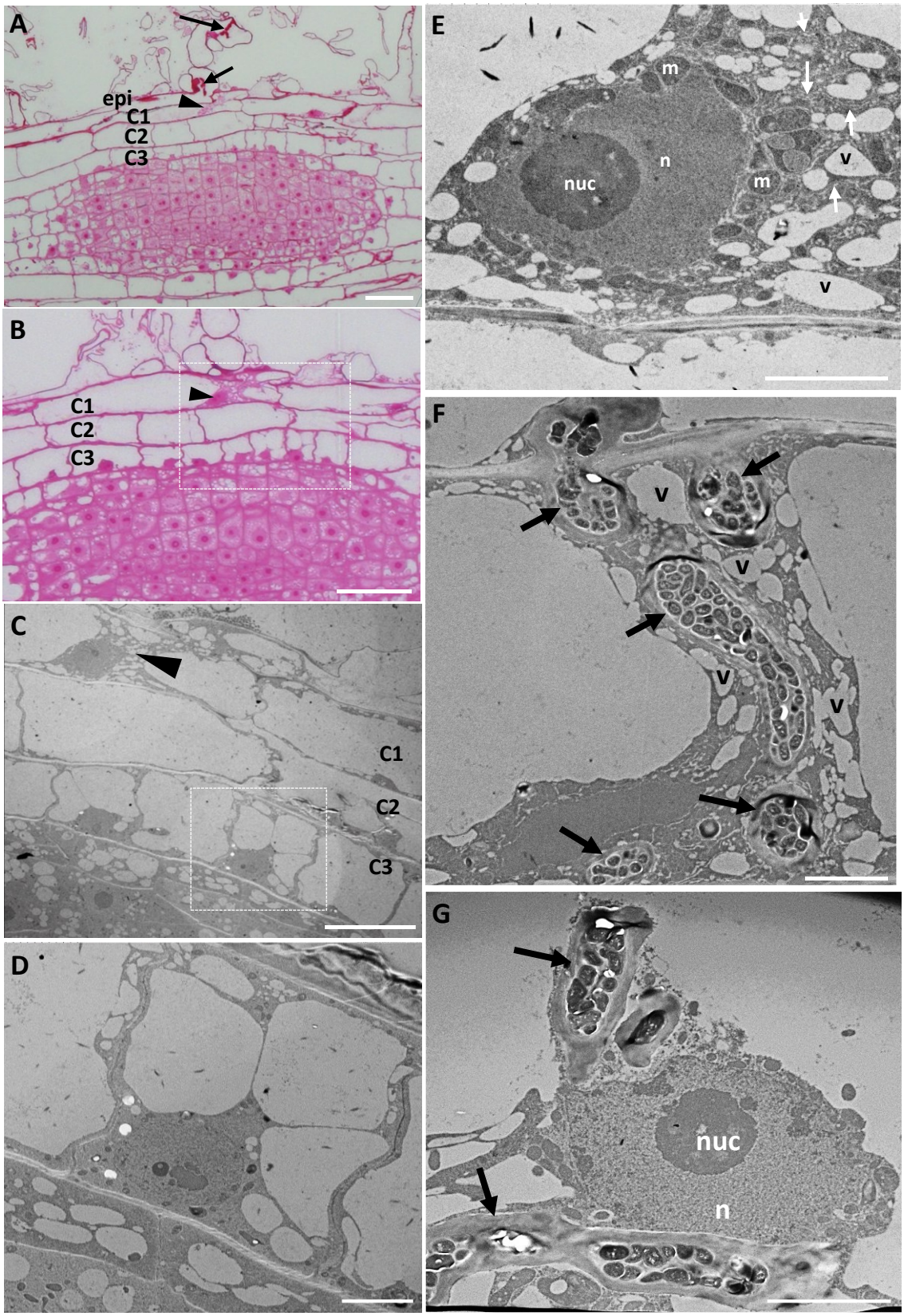

Fig. 1. Cell-specific structural changes in *M. truncatula* cells primed for infection.

(**A**-**B**) Representative images of longitudinal sections of *M. truncatula* roots 5 days after spot-inoculation with *S. meliloti.* These are consecutive 1 µm sections stained with basic fuchsin to reveal cell outlines and content. Arrows indicate ITs in root hair epidermal cells and

arrowheads indicate a C1 cortical cell exhibiting pre-infection priming. The region of interest in **B** (highlighted by a white square) is visualised in **C**-**E** by transmission electron microscopy of 80 nm sections. Note that the primed C1 outer cortical cell (arrowhead in **C**, and enlarged image in **E**) exhibits a unique structural organization compared with neighbouring cells. Primed cells comprise a cytoplasmic bridge enriched in endoplasmic reticulum (white arrows in **E**), and numerous vesicles or small vacuole-like (SV-like) structures (SVs) (v). They also have a large nucleus (n) surrounded by numerous mitochondria (m), a unique configuration not seen in other cells (for comparison, see C3 cells in **D** that will form the meristem). (**F**-**G**) At a later stage, when the IT (arrows) has progressed across the cytoplasmic bridge towards inner tissues, the nucleus is frequently found closely associated to the IT (**G**). Other abbreviations: nucleolus (nuc). Scale bars: **A**-**B** = 50 µm, **C** = 20 µm, **D**-**G** = 5 µm.

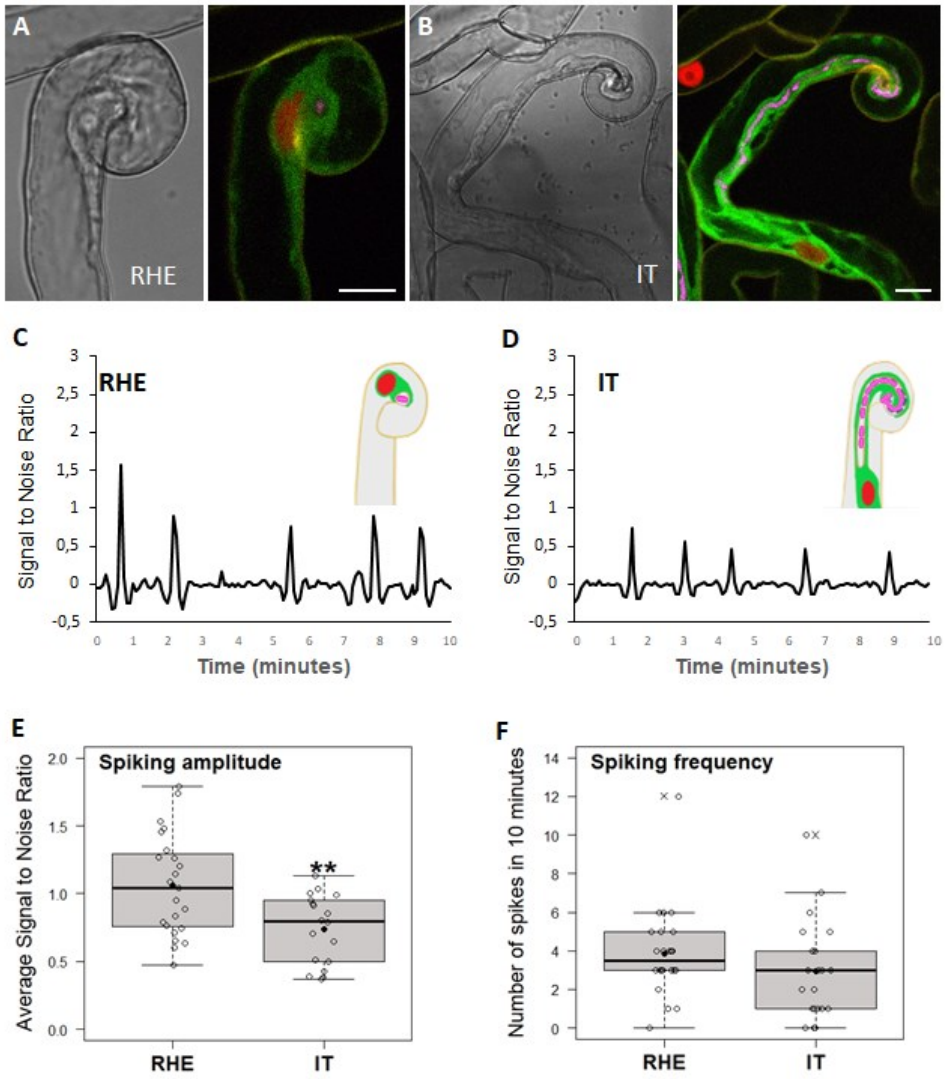

Fig. 2. Ca^{2+} spiking amplitude drops along root hair IT development.

(**A**-**B**) Representative bright-field and corresponding confocal images of (**A**) a root hair with entrapped CFP expressing (magenta)-*S. meliloti* (RHE) and (**B**) a root hair with a growing infection thread (IT) in *sunn-2*. Nuclei expressing the NR-GECO1 Ca^{2+} sensor appear in red, and the MtAnn1-GFP fluorescence (green) labels the cytoplasmic zone around the IT and the cytoplasmic bridge connecting and surrounding the nucleus. Scale bars: **A**-**B** = 10 µm. (**C**-**D**) Representative Ca^{2+} spiking traces of RHE (**C**) and growing IT stages (**D**). The relative concentration of Ca^{2+} ions in the nucleus is reflected by the intensity of NR-GECO1 fluorescence, expressed as signal-to-noise ratio (SNR, cf. Methods section). (**E**-**F**) Quantification of nuclear Ca^{2+} spiking: Spiking amplitude (**E**), expressed as average SNR of spikes per nucleus, and spiking frequency (**F**), expressed as number of spikes in 10 minutes per nucleus. Box plots represent the distribution of individual values (indicated by open circles) from root hairs with entrapped rhizobia (RHE, n=23 in **A** and n=24 in **F**) or with an IT (n=18 in **E** and n=21 in **F**) in *sunn2* 2-4 dpi with *S. meliloti* from three independent biological experiments. Median (central line), mean (solid black circle) and outliers (cross) are indicated. Two-tailed T-test (**E**) and Mann-Whitney test (**F**) of values were performed in R (asterisks indicate statistical difference; **$p < 0.01$). See also Figure S1 for Ca^{2+} spiking responses in *S. meliloti*-responsive root hairs of the nodulation-susceptible root zone in A17.

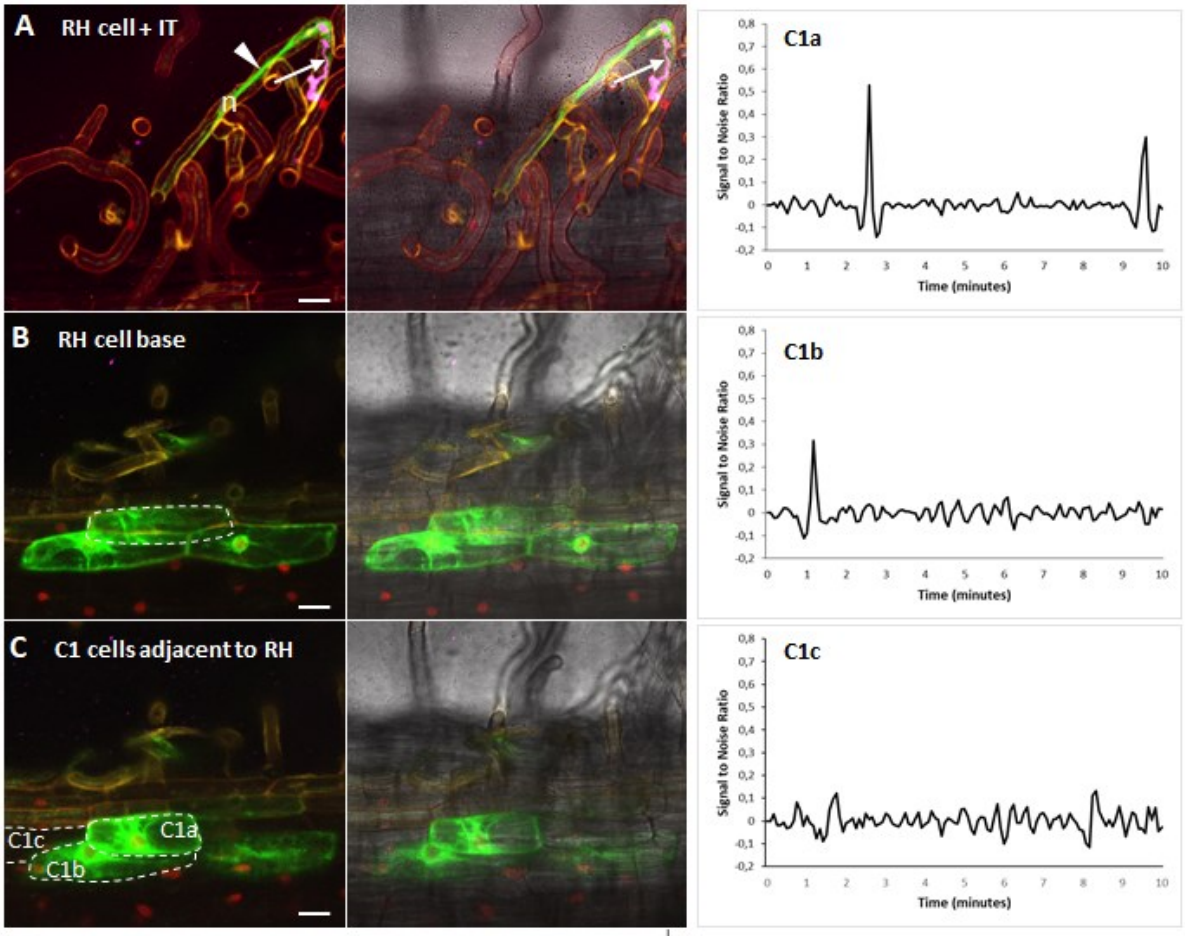

D

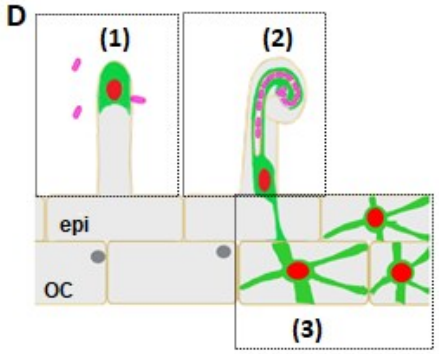

Genotypes	(1)	(2)	(3)	Sites	Reference
WT	+	+	+	11	this work
ern1	+	+	++[a]	14	this work
ern1 ern2	+	-	-	11	this work
dmi3	+	-	-	-	49
dmi3 + pEXPA-DMI3	+	+	-	11	this work

Fig. 3. Strong MtAnn1-GFP fusion fluorescence and low frequency Ca^{2+} spikes are hallmarks of pre-infection priming in the cortex.

Representative images of a root hair cell and neighbour outer cortex cells at a rhizobia infection site, in a root expressing MtAnn1-GFP (green) and NR-GECO1 (red). Confocal images from **A** to **C** illustrate the infected root hair with CFP-labelled rhizobia in IT (in magenta, arrow) and the nucleus (n) in front, guiding the growth of the IT in a cytoplasmic bridge (arrowhead) (**A**), the base of the RH cell (**B**, dotted line) and the neighbour C1a-c outer cortical cells (**C**, dotted lines). Images were obtained from A17 roots 4 dpi with *S. meliloti*. Representative traces of Ca^{2+} spiking from C1a, adjacent to the infected root hair, and neighbouring C1b and C1c cells. Note that only cortical cells co-expressing MtAnn1-GFP show detectable low frequency Ca^{2+} spiking (compare C1a-b and C1c). Traces are expressed as signal-to-noise ratio (SNR). (**D**) Genetic

dissection of pre-infection priming responses by co-expression of MtAnn1-GFP and NR-GECO1 in WT (A17 control) and in rhizobia-infection defective mutants (*ern1*, *ern1ern2*, *dmi3*). Left, schematic representation of Ca^{2+} spiking in *S. meliloti*-responsive non-infected root hairs of the nodulation-susceptible root zone (**1**), MtAnn1-GFP + Ca^{2+} spiking responses in infected root hairs (**2**) and infection primed cells in neighbouring epidermis or outer cortical cells (**3**) of the A17 WT control. Rhizobia are represented in pink, MtAnn1-GFP cytoplasmic labelling in green and nuclear Ca^{2+} spiking in red. Right, these responses are observed (+) or not (-) in different mutant backgrounds. All responses are observed in *ern1*, though deregulated (a) as indicated. Scale bars: **A**-**C** = 20 µm. See also Figures S1-S2.

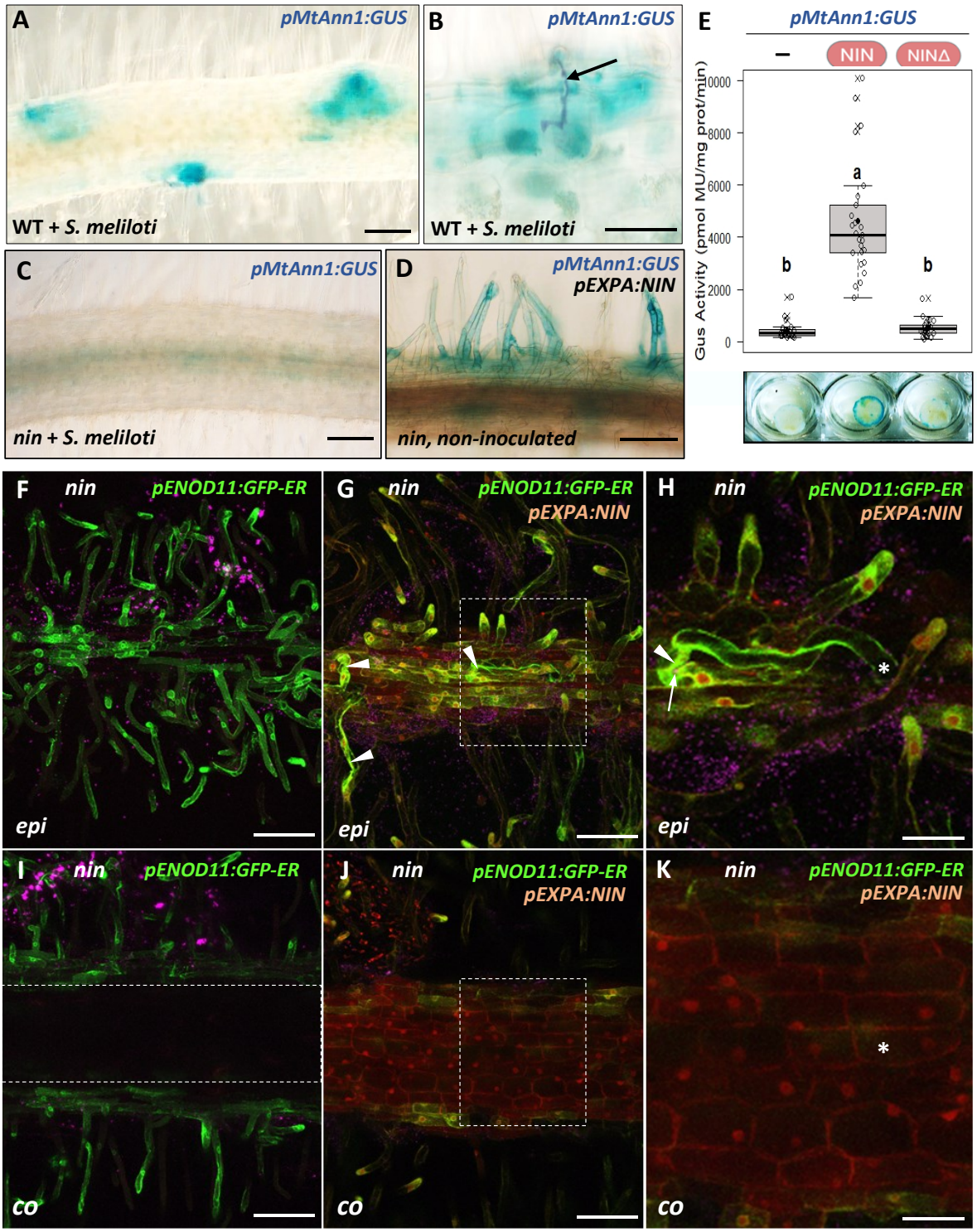

Fig. 4. NIN regulates cytoplasmic pre-infection priming and *MtAnn1* expression.

(**A**-**E**) Expression of the *pMtAnn1:GUS* fusion at infection sites in control WT (A17) roots at 4 dpi with *S. meliloti* (**A**-**B**). *LacZ*-expressing rhizobia are indicated in magenta (arrow) in **B**. This infection-related profile is abolished in *nin* (**C**). The expression of NIN under *pEXPA* induces the expression of the *pMtAnn1:GUS* fusion in the epidermis in the absence of rhizobia (**D**). Data in **A**-**D** are from two independent experiments (n=41 in A17, n=31 in *nin*, n=37 in *nin* + *pEXPA:NIN*). (**E**) Transactivation of the *pMtAnn1:GUS* fusion by NIN in *A. tumefaciens*-infiltrated leaf discs. Fluorimetric GUS assays were performed using 1 µg of total protein

extracts. Box plots represent the distribution of values (indicated as open circles) of individual plants (n=25 per sample) from 4 independent experiments. Median (central line), mean (solid black circle) and outliers (cross) are indicated. Different letters above the box blots indicate statistically significant difference (One-way ANOVA, α= 5%). Images of representative leaf discs are included. (**F**-**K**) *pENOD11:*GFP-ER expression in *nin* with or without epidermal-specific complementation with the *pEXPA:NIN* construct. Complemented roots (in **G**-**H**-**J**-**K**) co-express the *pUbiquitin*-driven fluorescent marker Ds-Red, which labels the cytosol and nucleoplasm in red. GFP-ER green fluorescence labels the perinuclear ER network, the tip of growing root hairs and the cytoplasmic column of primed root hair cells. In *nin* (**F**), GFP-ER labelling is only detected in perinuclear and root hair tip regions while in *nin* complemented with *pEXPA-NIN*, GFP-ER also labels cytoplasmic columns (arrowheads, **G** and **H**) in infection chamber-forming RHs (arrow in **H**). Adjacent OC1 cells show no green fluorescence in the cortex (see the boxed area in **I**) nor cytoplasmic reorganization (Ds-Red in **J**-**K**). **H** and **K** are boxed areas of **G** and **J**, respectively. Data were obtained from 2 independent experiments (n=19 for *nin* and n=19 for *nin* + *pEXPA:NIN*). Asterisks in **H** and **K** mark the xy position of the infected root hair base. Abbreviations: epi=epidermis; co=cortex. Scale bars: **A**, **C**, **D** = 100 µm, **B** = 50 µm, **F**, **G**, **I**, **J** = 100µm, **H**-**K** = 40 µm.

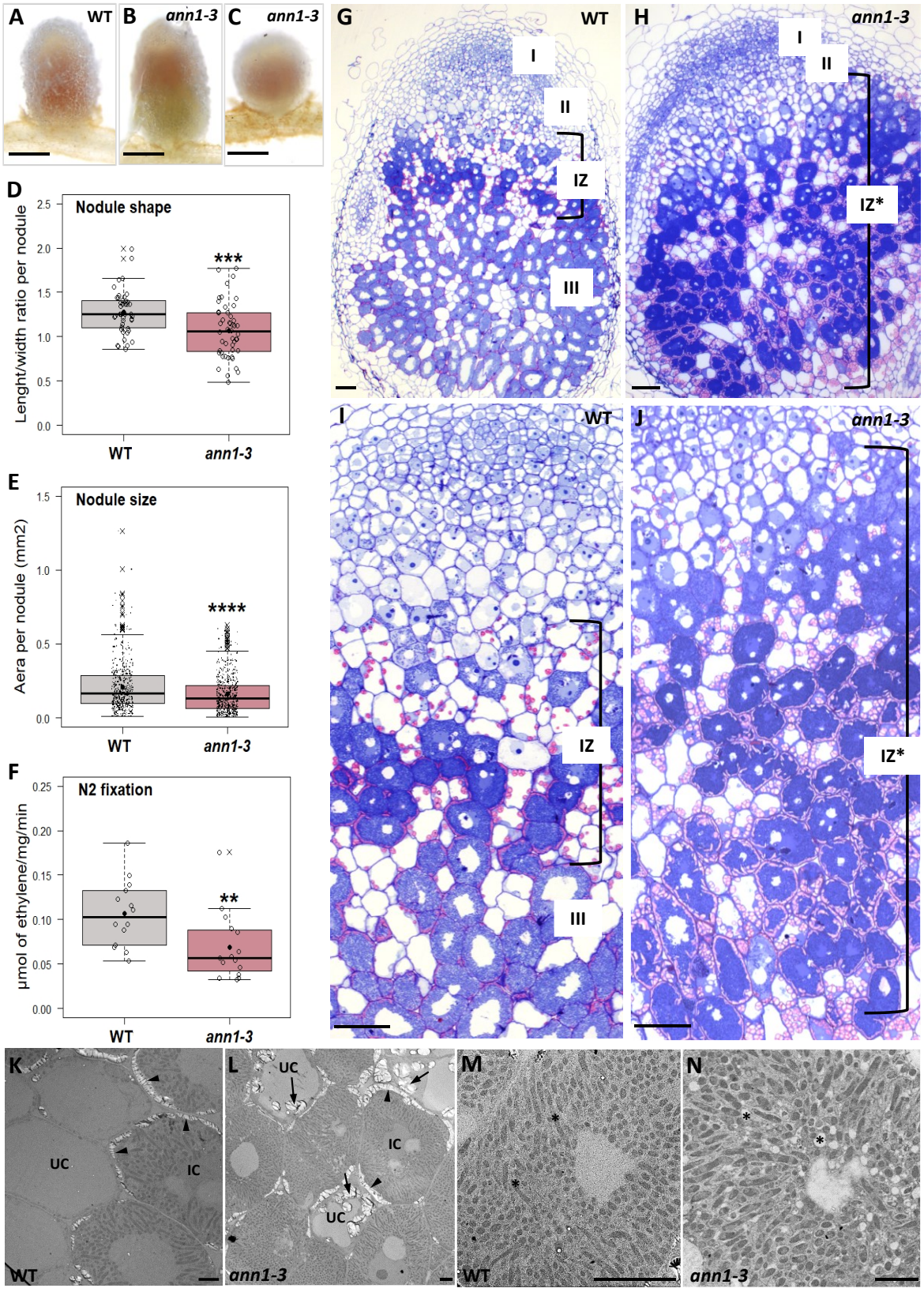

Fig. 5. *MtAnn1* mutants show impaired nodule differentiation and function.

(**A**-**C**) Representative images of mature nodules developed in WT (**A**) and *ann1-3* mutant (**B**-**C**) roots 21 dpi with *S. meliloti*. (**D**) Nodule shape, represented by the ratio of maximal length to maximal width of individual nodules, was measured on WT (n=43) and *ann1-3* (n=48) mutant

nodules from 3 independent experiments. (**E**) Automated measurements of nodule area by Image J were performed on individual nodules (10 dpi) from *ann1-3* (n=494 nodules from 48 roots) and WT (n=556 nodules from 42 roots) from 4 independent experiments. (**F**) Nitrogen fixation capacity was measured in nodulated root segments of *ann1-3* (n=15) and WT (n=14) collected 21 dpi with *S. meliloti* from 3 independent experiments (and comprising respectively 365 and 417 nodules). Box plots in **D**-**F** represent the distribution of individual values (indicated as open circles in **D** and **F**, and as black dots in **E**). Median (central line), mean (solid black circle) and outliers (crosses) are indicated. WT boxplots are in grey, *ann1-3* mutant boxplots are in dark pink. Two-tailed t-tests (in **D** and **F**) or a two-tailed Mann-Whitney test (in **E**) of values were performed in R (asterisks indicate statistical differences; ****p < 0.0001; ***p < 0.001; **p < 0.01). (**G**-**N**) Detailed views of WT R108 and *ann1-3* mutant 15 dpi nodule sections. (**G**-**J**) In 1µm longitudinal sections stained with toluidine blue/basic fuchsin, meristematic (I), infection (II), interzone (IZ) and nitrogen fixing (III) zones are distinguished in WT nodules (**G**, **I**). The amyloplast-rich IZ and zone III are clearly defined in WT, while *ann1-3* nodules (**H**, **J**) show a much larger IZ like region, with starch over-accumulation and no zone III comparable to that observed in WT nodules. (**K**-**N**) Ultrastructural analyses by TEM of WT and *ann1-3* nodules. (**K**, **M**) Close up view of zone III of a WT nodule with uninvaded cells (UC) and invaded cells (IC) filled with bacteroids (asterisks in **M**). Arrowheads indicate amyloplasts located near intercellular spaces of IC. (**L**, **N**) *ann1-3* nodules also include IC with apparent differentiated bacteroids. However, they appear as bacteroids typical of interzone II-III (Vasse et al), imbedded in a region enriched in white vesicles (black asterisks in **N**). *ann1-3* nodules accumulate amyloplasts not only in IC (arrowheads), but also in UC. Scale bars: **A**-**C** = 1 mm, **G**-**J** = 50 µm, **K**-**N** = 5 µm.

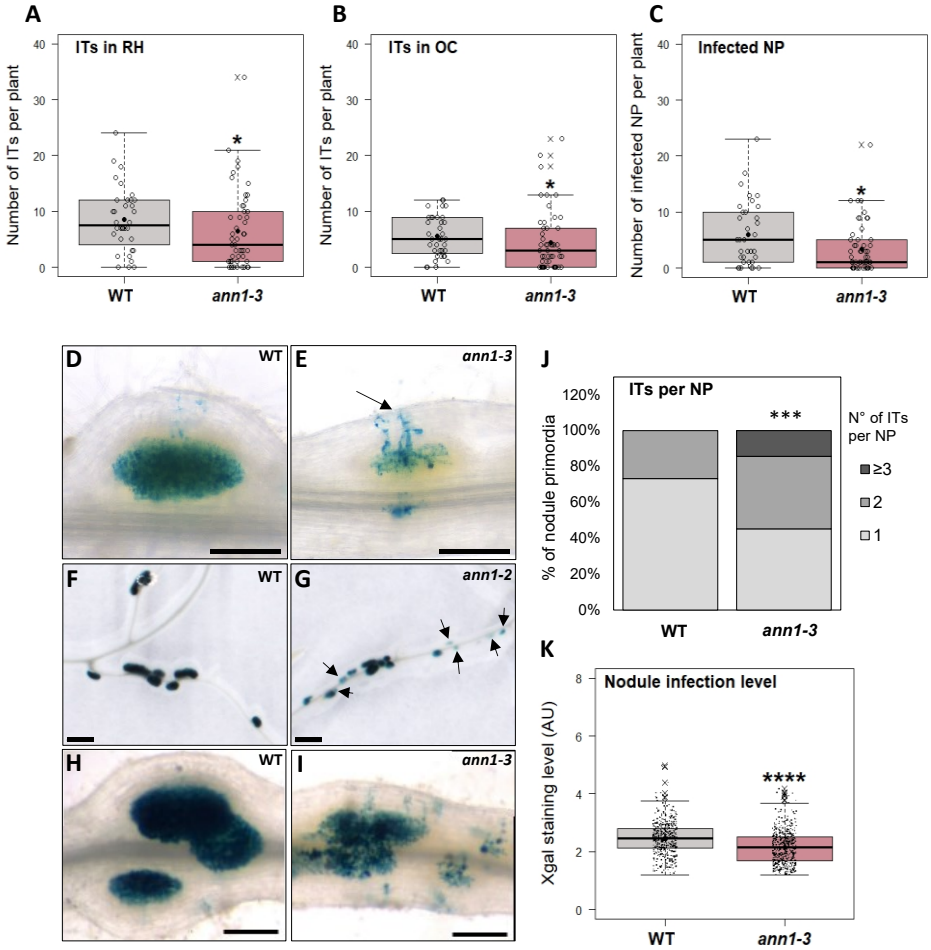

Fig. 6. Root Infection is negatively impacted in *ann1* mutants.

(**A**-**C**) Early root infection by rhizobia is less efficient in *ann1-3* than in WT at 4 dpi. Rhizobia infection was quantified in root systems of WT (n=36) and *ann1-3* (n=53) plants after histochemical X-gal staining to reveal infection events by *lacZ*-expressing *S. meliloti* rhizobia in blue. The number of root hairs with ITs (**A**), the number of infection sites with ITs that had reached the outer cortex (**B**) and the number of fully infected nodule primordia (**C**) were quantified from 3 independent experiments. Two-tailed Mann-Whitney tests of values in **A**-**C** were performed in R (asterisks indicate statistical differences, *p < 0.05; ***p < 0.001; ****p < 0.0001). (**D**-**I**) Representative images of WT and *ann1-2* or *ann1-3* infected nodules or emerging nodule primordia at 4 dpi (**D**-**E**) or 10 dpi (**F**-**I**). *ann1* mutant roots exhibit overall less colonized nodules (indicated by arrows in a global root view in **G**, and shown in close up views in **H** and **I**). (**J**) Frequency of nodule primordia at 4 dpi colonized by 1, 2 or 3 or more ITs. Colonization of *ann1* nodule primordia frequently occurs from 2 or more IT colonization sites compared with WT (arrowheads in **D**-**E**) (Chi square test, p=0.0005, ***). (**K**) Relative nodule infection level was quantified by automated ImageJ measurement of bacterial X-gal blue staining on 10 dpi nodules formed on WT (494 nodules from 48 plants) and *ann1-3* (556 nodules from 42 plants) roots. Box plots represent the distribution of individual values (indicated as open circles in **A-C**, and as black dots in **K**) from 4 independent experiments. A two-tailed Mann-Whitney test of values in R revealed significant differences (****p < 0.0001). Median (central line), mean (solid black circle) and outliers (cross) are indicated. WT is in grey, the *Mtann1-3* mutant is in dark pink. Scale bars: **D**-**E** = 250 µm, **F**-**G** = 1 mm, **H**-**I** = 1 mm.

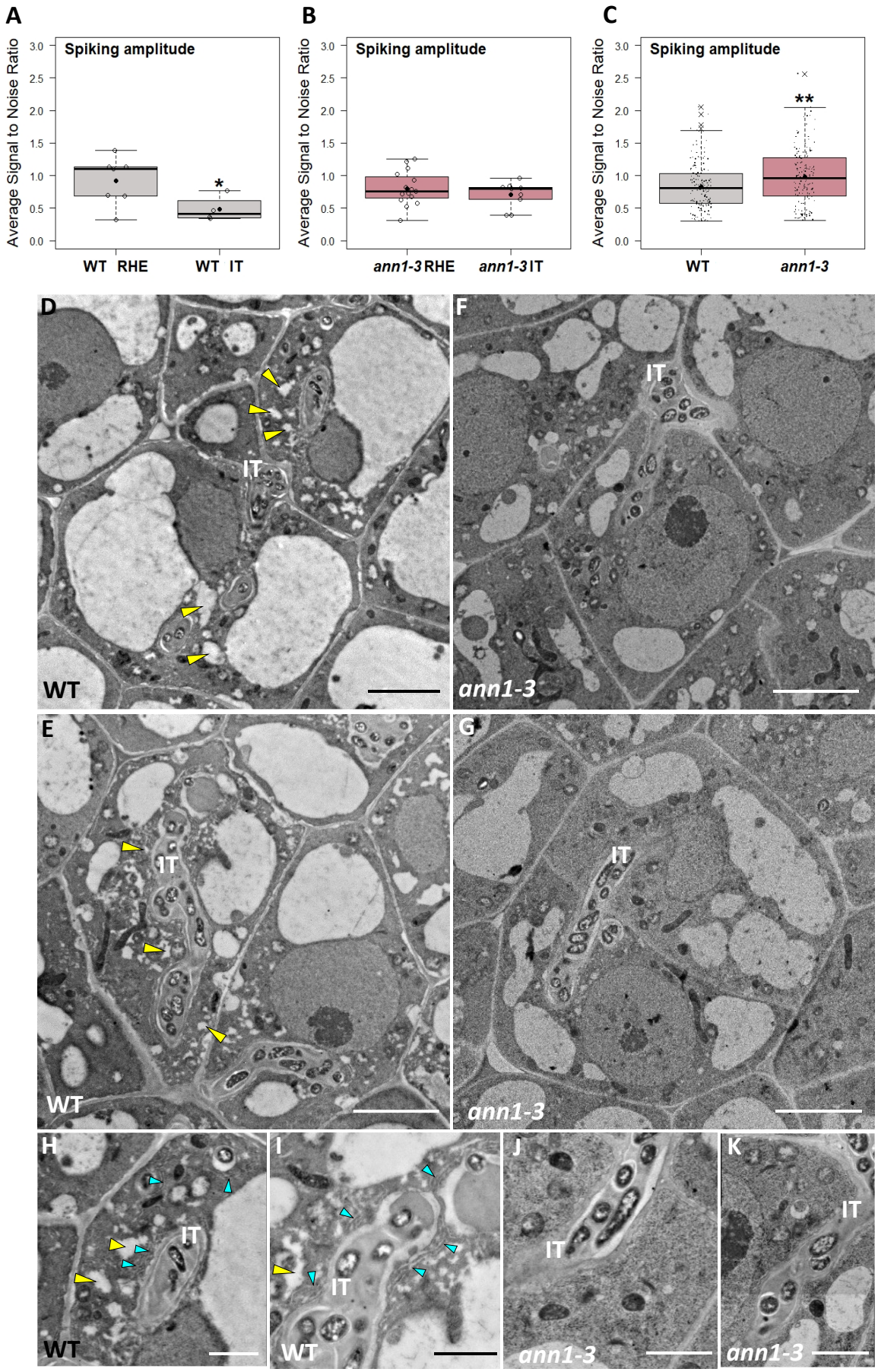

Fig. 7. Modified Ca^{2+} spiking and IT cytoplasmic environment in the absence of MtAnn1.

(**A**-**C**) Transgenic roots expressing the NR-GECO1 Ca^{2+} sensor, were generated to monitor nuclear Ca^{2+} oscillations in genetic backgrounds mutated (*ann1-3*) or not (WT) in *MtAnn1*. Variations in Ca^{2+} ion concentration, through changes in the relative intensity of NR-GECO1 fluorescence, is expressed as signal-to-noise ratio (SNR, cf. Methods section). Box plots represent average amplitude of spikes (spike SNR), calculated separately for each nucleus of root hairs with entrapped rhizobia (RHE) or with ITs in WT (WT RHE, n=7; WT root hairs with ITs, n=4) (**A**) or *ann1-3* (*ann1-3* RHE, n=15; *ann1-3* root hairs with ITs, n=9) (**B**) as well as *S. meliloti*-inoculated non-infected root hairs (**C**)(WT, n=160 and *ann1-3*, n=156) at 1-4 dpi. Data was obtained from three independent biological experiments. One-tailed t-tests (in **A**-**B**) and a bilateral Mann-Whitney test (in **C**) of values were performed in R (asterisks indicate significant differences, *p < 0.05; **p>0.01). Median (central line), mean (solid black circle) and outliers (cross) are indicated. WT is in grey, the *Mtann1-3* mutant is in dark pink. (**D**-**K**) Transmission electron microscopy analyses of infected cells from apical zone 2 of WT (**D**-**E**, **H**-**I**) or *ann1-3* (**F**-**G**, **J**-**K**) 15 dpi nodules. ITs in WT are embedded in vesicle-rich (yellow arrowheads) cytoplasmic bridges with visible ER network (blue arrowheads). These cytoplasmic features are not as prominently detected in *ann1-3*. Scale bars: **D**-**G** = 5 µm, **H**-**K** = 2 µm.

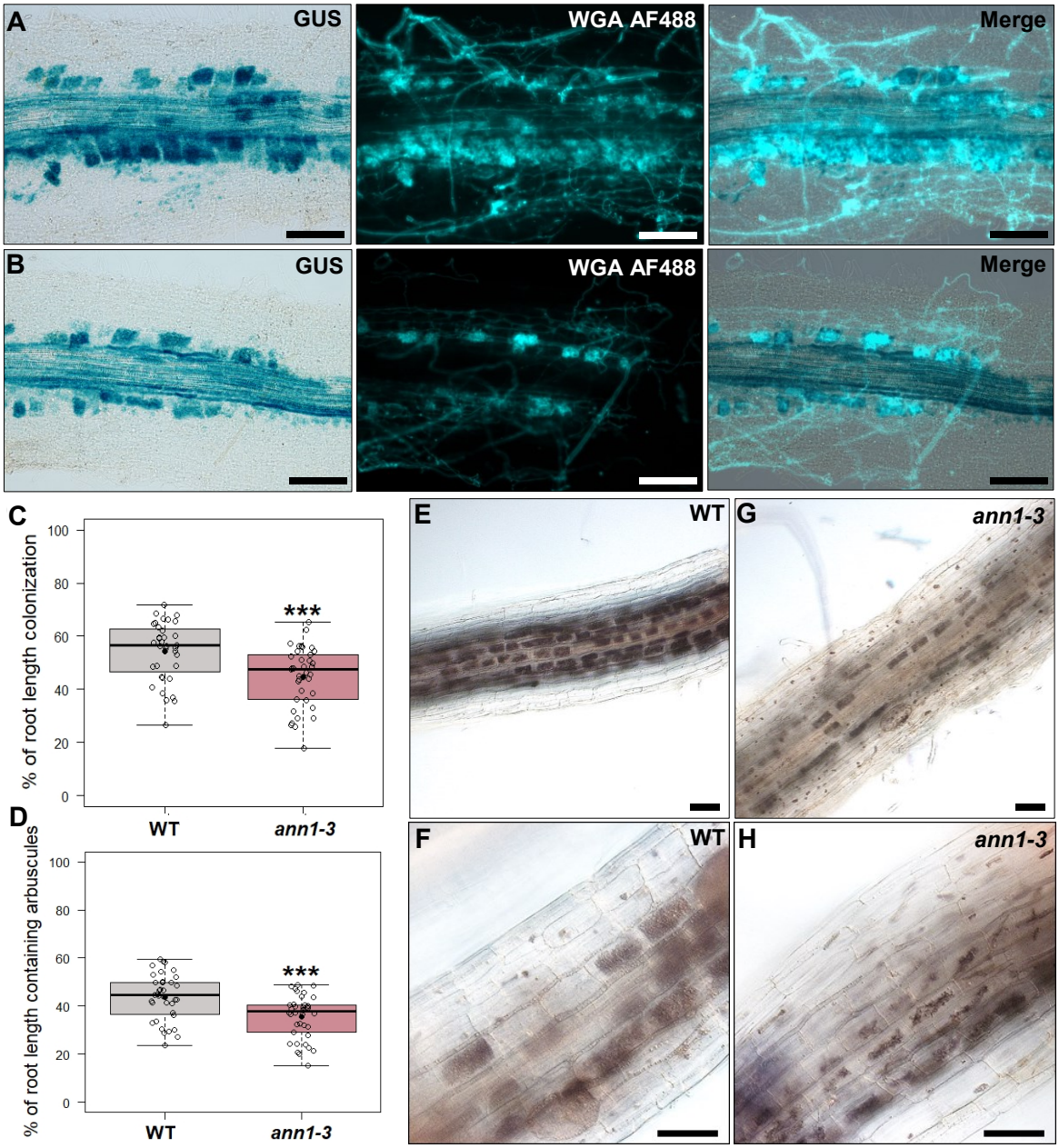

Fig. 8. *MtAnn1* is required for efficient mycorrhization *of M. truncatula* roots.

(**A-B**) *MtAnn1* promoter activity in independent *M. truncatula* roots colonized with *R. irregularis* at 4 wpi. Blue GUS staining correlates with *R. irregularis* colonized areas, visualized by WGA-AlexaFluor488 fluorescence staining. (**C-D**) Determination of intraradical colonization by *R. irregularis* in WT and *ann1-3* plants by the gridline intersect method. The relative surface of the root system displaying vesicles, arbuscules and/or intraradical hyphae is given in (**C**), while the relative surface corresponding specifically to arbuscules is given in (**D**). Box plots represent values from WT (n=36) and *ann1-3* (n=38) root systems at 6 weeks post-inoculation, from two independent biological experiments. Individual values (open circles), median (central line) and mean (solid black circle) are indicated. Two-tailed Student t-tests were performed. Asterisks indicate significant differences, ***p<0.001. (**E-H**) Representative pictures of ink

1295 stained AMF-colonized roots in WT (**E**-**F**) and *ann1-3* (**G**-**H**). Scale bars: **A**-**B** = 100 µm, **E**-**H**= 50
1296 µm.